Near-IR oxygen nightglow observed by VIRTIS in the Venus upper atmosphere

Giuseppe Piccioni, Ludmilla Zasova, Alessandra Migliorini, Pierre Drossart, Alexey V. Shakun, A. García Muñoz, Franklin P. Mills, Alejandro Cardesin Moinelo

Near-IR oxygen nightglow observed by VIRTIS in the Venus upper atmosphere

G. Piccioni,[1] L. Zasova,[2] A. Migliorini,[1] P. Drossart,[3] A. Shakun,[2] A. García Muñoz,[4] F. P. Mills,[4,5] and A. Cardesin-Moinelo[1]

Received 29 February 2008; revised 9 January 2009; accepted 17 February 2009; published 30 April 2009.

[1] We present observations of both the (0–0) and (0–1) bands at 1.27 and 1.58 μm of the $O_2(a^1\Delta_g - X^3\Sigma_g^-)$ nightglow made with the Visible and Infrared Thermal Imaging Spectrometer (VIRTIS) instrument aboard Venus Express. The observations were conducted in both nadir and limb viewing modes, the latter constituting the first systematic investigation into the vertical distribution of the volume emission rate of the infrared oxygen nightglow in Venus' upper atmosphere. Limb measurements from 42 orbits covering the latitude range 7°S to 77°N are analyzed. The peak altitude of the volume emission rate occurs typically between 95 and 100 km, with a mean of 97.4 ± 2.5 km. The vertical profile is broader near the equator, with a full width at half maximum of 11 km, a factor 2 larger than at middle latitudes. A double peak is frequently observed, with the lower and upper peaks occurring near 96–98 km and 103–105 km, respectively. On average, the nightglow appears brightest in the vicinity of the antisolar point. This conclusion is consistent with past ground-based observations and nadir measurements by VIRTIS. We mapped the global mean O_2 nightglow intensity from VIRTIS data collected during 880 orbits. Patchy features of the nightglow intensity observed in nadir view are correlated with the thermal brightness at 4.23–4.28 μm. The observed positive correlation is consistent with downwelling (upwelling) of oxygen atoms accompanying compressional heating (expansion cooling) or with modulation by gravity waves. Finally, from simultaneous measurements of the 1.27 and 1.58 μm bands, we have estimated the ratio of the transition probabilities A_{00}/A_{01} to be 63 ± 8.

Citation: Piccioni, G., L. Zasova, A. Migliorini, P. Drossart, A. Shakun, A. García Muñoz, F. P. Mills, and A. Cardesin-Moinelo (2009), Near-IR oxygen nightglow observed by VIRTIS in the Venus upper atmosphere, *J. Geophys. Res.*, *114*, E00B38, doi:10.1029/2008JE003133.

1. Introduction

[2] Intense nightglow emission in the (0–0) band of the O_2 ($a^1\Delta_g - X^3\Sigma_g^-$) electronic transition near 1.27 μm was first detected on Venus in 1975 [*Connes et al.*, 1979]. Subsequent ground-based observations of the airglow emission on the nightside (nightglow) have shown that the intensity and spatial distribution are highly variable on time scales of hours to days [*Crisp et al.*, 1996; *Ohtsuki et al.*, 2005, 2008; *Bailey et al.*, 2008]. Nadir-looking observations by the Visible and Infrared Thermal Imaging Spectrometer (VIRTIS) on Venus Express (VEX) have provided more detailed coverage of the morphology of the nightglow, and visual tracking of bright features has enabled the estimation of apparent motions [*Hueso et al.*, 2008]. Limb observations by VIRTIS of the O_2 nightglow [*Drossart et al.*, 2007a; *Gérard et al.*, 2008] provide a complementary view of the chemistry and dynamics of Venus' upper atmosphere by determining the vertical distribution of the O_2 nightglow. However, no systematic study of a large number of limb observations of the O_2 nightglow has been published to date. In this work, we examine limb observations spanning 7°S to 77°N latitude and 2000 to 0400 local times. These observations were collected during the period from July 2006 until August 2008. This much larger set of data has allowed us to determine how the vertical distribution of O_2 nightglow varies with latitude. We have also been able to make an observational estimate of the ratio of the transition probabilities for the (0–0) and (0–1) bands near 1.27 and 1.58 μm, respectively. Our results provide new observational insight into the chemical and dynamical processes occurring in Venus' upper atmosphere and new constraints on chemical transport models.

[3] On Venus' nightside, $O_2(a)$ is believed to be produced primarily via reaction (1) [e.g., *Connes et al.*, 1979; *Mills*

[1]INAF, Istituto di Astrofisica Spaziale e Fisica Cosmica, Rome, Italy.
[2]Space Research Institute of Russian Academy of Sciences, Moscow, Russia.
[3]LESIA, Observatoire de Paris, UPMC, Université Paris-Diderot, CNRS, Meudon, France.
[4]Research School of Physics and Engineering, Australian National University, Canberra, ACT, Australia.
[5]Fenner School of Environment and Society, Australian National University, Canberra, ACT, Australia.

0148-0227/09/2008JE003133

and Allen, 2007], where O_2^* denotes an electronically excited state of O_2:

$$2O + M \rightarrow O_2^* + M \quad (1a)$$

$$O_2^* + M \rightarrow O_2(a) + M \quad (1b)$$

There are two recent estimates of the net yield of O_2(a) from reaction (1). *Crisp et al.* [1996] inferred net yields of 0.63 ± 0.19 and ∼0.6–0.75 for M = N_2 and CO_2, respectively, on the basis of laboratory studies, while *Huestis* [2002] recommends a net yield of 0.94–0.99 for M = N_2 and CO_2 on the basis of a combination of laboratory and atmospheric studies. The atomic oxygen consumed in reaction (1) is transported to the nightside via the upper atmospheric circulation from the dayside [*Bougher and Borucki*, 1994] where atomic oxygen is produced by photodissociation of CO_2 at wavelengths ∼<200 nm. Nightglow in the O_2(a-X) bands results from O_2 radiatively decaying from the electronically excited O_2(a) state to the ground electronic state. The vertical profile of the a-X nightglow is determined by the balance between production of O_2(a) via reaction (1) and its loss due to radiative decay of the O_2(a) state and collisional quenching. There has been controversy over the lifetime of O_2(a) against radiative decay, but recent laboratory measurements [*Cheah et al.*, 2000; *Lafferty et al.*, 1998; *Miller et al.*, 2001; *Newman et al.*, 1999; *Spalek et al.*, 1999] appear to have converged to a consistent value. The mean lifetime we have computed from these studies, 74 ± 3 min is consistent with recent assessments [*Gamache and Goldman*, 2001; *Slanger and Copeland*, 2003]. Only an upper limit on the rate constant for collisional quenching of O_2(a) by CO_2 has been determined in laboratory studies [*Sander et al.*, 2006], so coordinated limb observations of the O_2(a-X) nightglow, total density, and temperature may provide the best estimate to date of this rate constant. A recent calculation estimated ∼80% of the O_2(a) produced at ∼96-km altitude decay via emission in the a-X bands [*Gérard et al.*, 2008]. More detailed studies of VIRTIS' limb observations of O_2(a-X) nightglow should provide further insight into both the physical and chemical conditions in the nightglow region and the processes involved.

[4] The upper atmospheric circulation on Venus is a composite of two patterns: a subsolar (SS) to antisolar (AS) flow and a retrograde zonal flow. Long-term averages of NO and O_2 nightglow emissions suggest that the long-term average circulation at 115–150 km altitude is dominated by strong subsolar to antisolar flow with a weaker retrograde zonal flow [*Bougher and Borucki*, 1994]. Tracking of cloud features at 65–70 km shows the cloud top circulation is dominated by the retrograde zonal flow [*Gierasch et al.*, 1997; *Markiewicz et al.*, 2007; *Limaye*, 2007; *Sánchez-Lavega et al.*, 2008]. At intermediate altitudes, the relative strength of these two patterns varies with altitude and with time [*Lellouch et al.*, 1997; *Bougher et al.*, 2006]. Part of the temporal variability is likely due to breaking gravity waves transporting energy and momentum upward from the cloud tops [*Alexander*, 1992], but significant further work is required to understand and quantify their effects [*Bougher et al.*, 2006]. VIRTIS' limb observations of O_2(a-X) nightglow may provide insight into the vertical and horizontal transport processes and rates, complementing the horizontal transport results obtained using nadir-looking images from VIRTIS [*Hueso et al.*, 2008].

[5] The first reported detection of nightglow emission in the a-X (0–1) band of O_2 near 1.58 μm on Venus was based on VIRTIS data [*Piccioni et al.*, 2008]. This band has not been observed on Mars but has been observed on Earth [*Vallance Jones and Harrison*, 1958; *Winick et al.*, 1985]. No prior observation on any planet, however, has detected simultaneously the a-X (0–0) and (0–1) bands. Significant uncertainties exist in both laboratory and theoretical determinations of the relative transition probabilities for these bands, so VIRTIS' observations of the two bands should advance our understanding of the molecular physics of the a and X states of O_2.

2. Instrument Description and Observation Geometry

[6] VIRTIS is an imaging spectrometer which covers the spectral range 0.27 to 5.1 μm [*Piccioni et al.*, 2009; *Drossart et al.*, 2007b]. It includes two spectrometers: VIRTIS-M, a mapping spectrometer with medium spectral resolution, and VIRTIS-H, an echelle spectrometer with higher spectral resolution than VIRTIS–M but no imaging capability. VIRTIS-M includes two channels: a visible channel spanning 0.27 to 1 μm and an infrared channel spanning 1 to 5.1 μm. The results reported here were obtained using the infrared channel of VIRTIS-M, with spectral sampling interval of about 10 nm, a spectral full width at half maximum (FWHM) of about 15 nm, and an instantaneous field of view (IFOV) of 250 μrad. As is typical for an imaging spectrometer, a single instantaneous acquisition by VIRTIS-M collects a frame, which is composed of 432 bands (wavelengths) for each of 256 samples (spatial pixels along the instrument slit). If the slit is oriented perpendicular to the limb of Venus, then a single limb observation will obtain a full spectrum at each of 256 tangent altitudes, so the limb profiles of the a-X (0–0) and (0–1) nightglow emissions can be derived from a single frame. A scanning mirror (or the spacecraft's motion) is used to image multiple sites with different latitudes, longitudes, and/or local times and, thus, obtain a vertical cross section of the line of sight integrated nightglow emission. A similar process is used in nadir imaging mode to obtain 256 pixel × 256 pixel × 432 band spectral imaging cubes. A full spatial scan across the 64-mrad field of view (FOV) of the mirror requires around 50 min with an 8-s exposure time for each frame. The mirror moves nominally by 250 μrad during the acquisition of an 8-s frame, so that the typical pixel is square, but both the mirror's scan rate and the integration time can be varied. The orientation of the VIRTIS-M slit is fixed relative to the spacecraft, so it is not always possible to orient the VIRTIS-M slit perpendicular to Venus' limb when conducting limb observations. The least favorable observation geometry is when the VIRTIS-M slit is tangential to Venus' limb because then every spatial pixel samples approximately the same tangent altitude. However, even a 10° angle between the VIRTIS-M slit and Venus' limb is sufficient to obtain a nearly complete limb profile.

The absolute pointing accuracy for each pixel is much better than the IFOV. This is achieved thanks to the three-axis stabilized capability of the Venus Express spacecraft, supported by accurate star trackers which provide an absolute pointing accuracy better than ±35 μrad (about ±1/7 of a VIRTIS-M pixel) in the timeframe of the observation. Other observation geometries are possible [*Titov et al.*, 2006].

[7] Limb and nadir observations provide complementary information on nightglow emissions. During limb observations, the line of sight integrated volume emission is about 50 times larger than in nadir mode, so faint emissions from minor species are more easily detected. The vertical spatial resolution (2.5 km at 10,000-km slant distance), however, limits the maximum distance from which high-quality limb observations can be made. Venus Express' polar orbit has its pericenter at about 75°N, so almost all limb observations are made in the northern hemisphere. Nadir observations provide an extended view of the geographic distribution of nightglow emission but no information on its vertical distribution. Spatial resolution decreases when the spacecraft is further from Venus (15 km at apocenter), but areal coverage increases, so nadir observations are typically made over the southern hemisphere and areal coverage is extremely poor north of 20°N. Examples of observations in limb and nadir modes are shown in Figure 1 for orbits 76_18, 271_09, and 44_01 (prefix before the underscore is orbit number, suffix is session number, which is the period of time of continuous acquisition of data resulting in a spectral imaging cube). Figures 1a and 1b show an example of an observation made with the VIRTIS-M slit nearly perpendicular (in the central part of the scan, executed from top to bottom) and tangent to Venus' limb, respectively. Figure 1c (right) shows an example of nadir view.

3. Data Selection

[8] For this study, we have used both limb and nadir observations. The limb observations were acquired during 72 sessions from 42 orbits between July 2006 and August 2008, Table 1. Each orbit lasts 24 h and orbit number 5, the first stabilized nominal orbit, corresponds to 25 April 2006. Usually a few sessions are acquired within a single orbit. Each spectral imaging cube typically extends over 30° latitude, and the 72 sessions selected span 7°S to 77°N. These 72 sessions include all VIRTIS-M limb observations with exposure time of 8 s. Long exposure times (8 s) provide an excellent signal-to-noise ratio (SNR), typically better than 100, at wavelengths shorter than 4 μm, which enabled derivation of well defined vertical profiles, including the high-altitude tail, for fainter nightglow emissions, such as the a-X (0–1) band at 1.58 μm. The data from the 72 sessions selected have a vertical spatial resolution of about 2 km. The limb profiles of the O_2 emission are obtained for each 5° latitude interval as the moving average within 1 km of altitude (in vertical direction). Vertical profiles are retrieved from the observed limb profiles using an onion peeling technique. Most of the limb mode observations in Table 1 had a limb profile with a single peak. These observations were used for retrieval and study of the emission layer's characteristics. In Table 1 we report only the average of the parameters for each session. The three limb profiles in Table 1, selected as an example among the many others with double peaks but not reported, are discussed below but were not used for our statistical analyses.

[9] The nadir observations that were examined in greatest detail in this study are reported in Table 1. For simplicity here we call "nadir observations" all those where the instrument line of sight (LOS) intercepts the solid body of the planet, although the term "nadir" is more appropriate for perpendicular view only. All have exposure times of 3 to 18 s, since the a-X(0–0) band at 1.27 μm is sufficiently bright to provide enough signal for mapping its geographic distribution with these exposure times. The spatial resolution for the selected nadir observations is typically about 10 km.

[10] The global nadir view map for nightglow was constructed using all data collected during 880 orbits between 14 May 2006 and 14 September 2008 with emergence angle less than 80° (0° = nadir). The spanned period corresponds to about 4 Venusian years. The oxygen nightglow map was constructed from observations with exposure times of at least 0.1 s.

4. Data Processing and Separation of Thermal and Nightglow Emissions

[11] Nightside infrared spectra of Venus contain nightglow emission from multiple species and thermal emission, which originates in the lower atmosphere [*Allen and Crawford*, 1984]. In the spectral regions where absorption by CO_2 is small, the thermal emission can be observed outside Venus' atmosphere after having undergone multiple scattering within Venus' cloud layers [*Kamp et al.*, 1988]. One window in the CO_2 absorption spectrum lies near 1.27 μm [*Meadows and Crisp*, 1996], so emission originating from below 20 km altitude [*Tsang et al.*, 2008] and scattered by higher-altitude clouds overlaps spectrally and, for nadir observations, spatially with the a-X(0–0) nightglow emission. Although the peak of the a-X(0–0) nightglow emission occurs at a shorter wavelength than the maximum of the thermal emission, it is not possible to spectrally resolve and quantitatively separate the two sources with VIRTIS-M's spectral resolution. However, nearby spectral windows, at 1.18 and 1.74 μm, provide information on the thermal emission from the lower atmosphere that may be used to assess the contribution of thermal emission to the observed 1.27 μm radiance and to empirically remove the thermal emission contribution when significant. The nightside radiance at 1.18 μm originates from the surface and the lowest 20 km of the atmosphere [*Meadows and Crisp*, 1996]. The 1.74 μm radiance originates from near 20–28 km [*Meadows and Crisp*, 1996]. Given existing uncertainties in the CO_2 spectrum near 1.27 μm [*Tsang et al.*, 2008], an empirical approach for removing the thermal emission contribution at 1.27 μm is probably as accurate as more detailed radiative transfer calculations.

[12] For limb observations, as shown in Figure 2a, the thermal emission at 1.18 and 1.74 μm is much smaller than the radiance at 1.27 μm between 90 and 103 km. The difference is attributed to the nightglow and therefore, given the expected correlation among these bands for the thermal emission, it is safe to neglect the thermal emission at 1.27 μm in this altitude range. Some typical limb profiles of the oxygen nightglow intensity at 1.27 μm are shown in

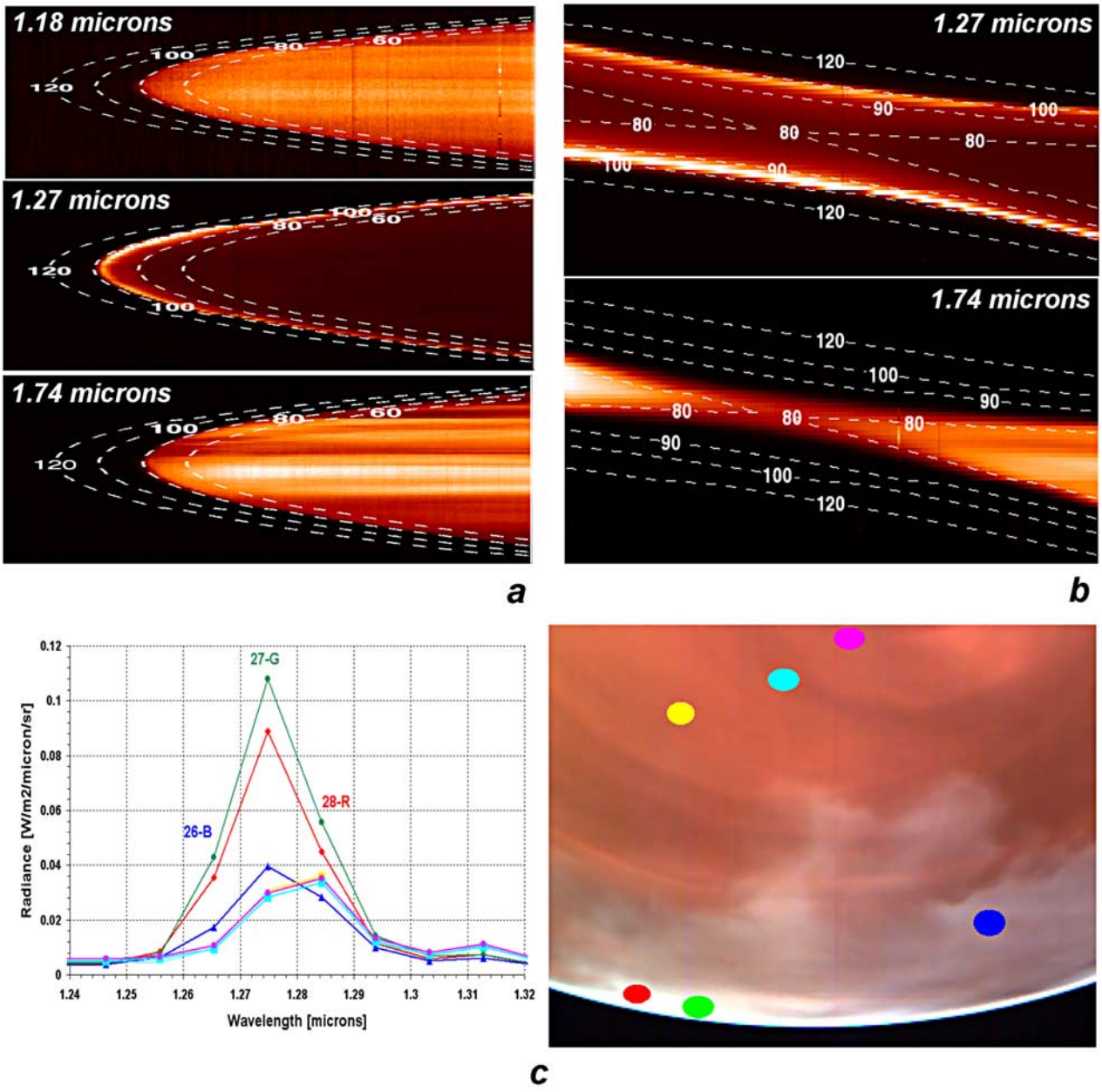

Figure 1. Limb and nadir view modes. (a) Orbit 76_18, case of limb observation with slit (parallel to the horizontal direction) almost perpendicular to the limb in the central part of the image. The image of the oxygen nightglow emission at 1.27 μm and the images in 1.18 and 1.74 μm (thermal emission of the lower atmosphere scattered by the clouds) windows are shown. The isolines are the tangent altitude above the Venus ellipsoid. Scattered thermal emission extends up to altitudes exceeding 80 km. (b) Orbit 271_09, case of limb observation with slit approximately parallel to the limb. (top) Image at 1.27 μm. (bottom) Image of the same cube but at 1.74 μm, same scale. The isolines are the tangent altitude. (c) Orbit 44_01, case of nadir mode. Several spectra in the 1.27 μm range are shown for different points of the image. Different colors of spectra coincide with the same color of area in the red-green-blue (RGB) image. Positions of the R, G, and B bands are shown on the spectra. The area of O_2 emission appears white in this composite. The shift to shorter wavelengths of the nightglow maximum emission compared to the maximum of the thermal emission from below the clouds can be seen (compare for example the green and magenta spectra). The small peak in the spectra at about 1.31 μm is a thermal emission in another atmospheric window.

Table 1. Summary of the Selected Data[a]

					Volume Emission Rate			
Limb Session	Start Time	Latitude Range (deg)	Local Time Range (h)	Peak From Limb (km)	Peak (km)	FWHM (km)	Peak Intensity (MR/km)	Total VER (MR)
VI0076_18[b]	2006-07-06T01:34:11.885	30.0:65.0	21.8:23.9	95.6	96.7	3.9	0.06	0.27
VI0271_09	2007-01-17T07:36:25.808	15.0:35.0	23.8:2.4	95.7	97.3	5.7	0.14	0.91
VI0275_06	2007-01-21T07:33:11.848	15.0:40.0	0.3:2.9	94.5	97.3	6.3	0.06	0.43
VI0317_06[b]	2007-03-04T06:12:02.447	15.0:30.0	23.8:0.7	94.3	96.0	9.7	0.12	1.10
VI0317_07[b]	2007-03-04T06:26:02.459	25.0:50.0	23.7:0.4	94.2	96.6	9.0	0.05	0.49
VI0317_08[b]	2007-03-04T06:40:02.483	50.0:75.0	0.03:7.1	95.2	97.4	5.8	0.04	0.26
VI0320_03[b]	2007-03-07T06:09:36.409	15.0:35.0	0.18:1.1	93.0	95.3	8.5	0.03	0.31
VI0320_04[b]	2007-03-07T06:23:36.415	25.0:50.0	0:0.8	94.8	96.2	6.2	0.04	0.26
VI0321_03[b]	2007-03-08T06:08:48.416	15.0:30.0	0.31:1.2	92.3	95.3	9.3	0.03	0.29
VI0321_04[b]	2007-03-08T06:22:48.431	25.0:50.0	0.1:0.9	96.0	98.3	8.7	0.06	0.45
VI0321_05[b]	2007-03-08T06:36:48.443	50.0:75.0	0.46:7.4	98.2	101.4	6.4	0.13	0.85
VI0322_06[b]	2007-03-09T06:07:58.525	15.0:30.0	0.43:1.3	92.7	96.3	9.3	0.03	0.25
VI0322_07[b]	2007-03-09T06:21:58.413	25.0:50.0	0.21:0.97	96.4	99.4	6.6	0.03	0.24
VI0322_08[b]	2007-03-09T06:35:58.536	60.0:70.0	0.57:7.5	98.0	101.0	5.0	0.09	0.47
VI0323_07[b]	2007-03-10T06:21:10.344	30.0:50.0	0.32:1.08	96.5	99.8	6.3	0.08	0.64
VI0323_08[b]	2007-03-10T06:35:10.475	50.0:60.0	0.68:7.6	97.0	101.0	7.0	0.14	1.01
VI0324_06[b]	2007-03-11T06:06:22.483	15.0:30.0	0.67:1.5	96.7	98.7	9.3	0.10	0.96
VI0324_07[b]	2007-03-11T06:20:22.504	25.0:50.0	0.43:1.2	96.8	99.6	7.8	0.08	0.59
VI0324_08[b]	2007-03-11T06:34:22.594	50.0:60.0	0.78:7.7	98.0	101.0	8.0	0.08	0.58
VI0327_05[b]	2007-03-14T06:03:57.504	15.0:30.0	1.05:1.8	96.3	101.0	11.0	0.12	1.19
VI0327_06[b]	2007-03-14T06:17:56.492	35.0:50.0	0.77:1.5	93.3	95.0	7.3	0.03	0.28
VI0327_07	2007-03-14T06:31:57.442	50.0:75.0	1.11:7.99	93.2	94.6	6.4	0.02	0.10
VI0330_04[b]	2007-03-17T06:01:32.528	15.0:30.0	1.4:2.1	92.7	95.7	9.7	0.02	0.23
VI0330_05[b]	2007-03-17T06:15:32.429	25.0:45.0	1.1:1.8	93.3	95.0	7.0	0.03	0.21
VI0330_06	2007-03-17T06:29:32.559	50.0:75.0	1.4:8.26	93.8	95.4	5.6	0.02	0.11
VI0364_07	2007-04-20T05:36:38.960	15.0:30.0	21.4:21.9	97.3	99.7	7.7	0.09	0.73
VI0364_08	2007-04-20T05:50:45.877	30.0:45.0	21.6:22.3	97.0	99.3	7.0	0.11	0.77
VI0364_09	2007-04-20T06:04:52.891	55.0:65.0	17.8:21.8	98.0	98.5	3.5	0.10	0.48
VI0371_10[b]	2007-04-27T05:42:00.927	35.0:60.0	21.9:23.5	97.2	99.6	5.6	0.11	0.78
VI0377_11[b]	2007-05-03T05:37:23.199	35.0:60.0	22.6:0.16	97.0	99.6	7.4	0.10	0.81
VI0383_12	2007-05-09T05:51:47.236	35.0:50.0	18.03:0.8	94.0	95.3	6.7	0.04	0.29
VI0443_06[b]	2007-07-08T07:36:05.904	0.0:20.0	0.9:2.86	94.8	98.3	9.8	0.11	1.03
VI0449_10[b]	2007-07-14T07:38:35.961	0.0:20.0	1.6:3.5	92.5	95.8	10.3	0.08	0.90
VI0457_08	2007-07-22T07:14:22.048	0.0:25.0	19.2:21.0	93.0	96.6	10.0	0.01	0.12
VI0460_08	2007-07-25T06:58:28.022	0.0:25.0	19.5:21.4	93.2	96.4	10.4	0.01	0.13
VI0461_07	2007-07-26T06:53:09.967	0.0:25.0	19.6:21.5	93.8	97.0	9.8	0.02	0.17
VI0499_11[b]	2007-09-02T03:13:58.502	10.0:40.0	23.9:3.1	98.8	100.2	6.5	0.10	0.71
VI0507_11	2007-09-10T02:34:10.606	10.0:40.0	0.8:3.3	98.5	100.3	7.2	0.11	0.87
VI0507_12[b]	2007-09-10T03:07:10.565	0.0:20.0	23.6:1.7	94.8	98.3	10.3	0.11	1.16
VI0516_05[b]	2007-09-19T02:04:08.786	0.0:30.0	0.9:3.0	94.7	96.8	9.7	0.10	1.03
VI0517_05[b]	2007-09-20T01:58:48.667	0.0:25.0	1.0:3.1	94.8	97.0	9.0	0.15	1.30
VI0519_05[b]	2007-09-22T01:53:38.770	0.0:25.0	1.3:3.4	95.4	98.2	8.0	0.12	0.99
VI0565_18[b]	2007-11-07T00:50:16.235	10.0:15.0	2.6:3.5	100.0	103.0	9.0	0.09	0.86
VI0565_19[b]	2007-11-07T01:12:15.305	25.0:40.0	2.0:2.9	97.3	98.7	6.0	0.04	0.27
VI0565_20[b]	2007-11-07T01:26:16.217	45.0:70.0	2.2:5.1	93.0	95.0	7.4	0.01	0.10
VI0600_00	2007-12-12T02:07:05.806	10.0:25.0	22.2:23.5	96.3	99.3	8.0	0.08	0.74
VI0600_02[b]	2007-12-12T02:45:05.782	50.0:65.0	20.2:23.7	100.3	101.3	3.7	0.14	0.69
VI0602_00	2007-12-14T02:10:56.781	10.0:25.0	22.4:23.7	97.0	101.7	11.0	0.06	0.68
VI0602_02[b]	2007-12-14T02:48:55.817	50.0:75.0	20.4:23.9	93.2	94.4	5.4	0.02	0.15
VI0623_00	2008-01-04T02:56:19.960	10.0:25.0	0.8:2.2	93.3	96.7	9.3	0.03	0.32
VI0623_01[b]	2008-01-04T03:14:19.984	20.0:50.0	1.4:2.4	95.0	97.3	7.3	0.06	0.44
VI0718_03	2008-04-08T04:36:17.693	0.0:20.0	22.4:0.3	93.5	98.0	11.0	0.05	0.58
VI0724_02	2008-04-14T04:30:38.081	0.0:5.0	22.4:0.8	94.5	98.5	12.5	0.10	1.32
VI0733_02	2008-04-23T04:06:09.731	5.0:30.0	0.7:2.2	97.6	99.8	8.4	0.14	1.28
VI0742_02	2008-05-02T04:20:36.192	5.0:15.0	1.3:2.9	94.5	97.5	10.0	0.07	0.73
VI0754_01	2008-05-14T02:54:24.287	25.0:45.0	22.0:23.0	93.5	95.8	7.3	0.06	0.47
VI0754_02	2008-05-14T03:08:24.287	45.0:70.0	22.2:0.7	93.0	95.0	6.5	0.01	0.11
VI0764_01	2008-05-24T03:02:37.862	25.0:45.0	23.1:0.1	93.0	95.8	8.8	0.03	0.26
VI0764_02	2008-05-24T03:16:38.266	45.0:70.0	23.2:1.9	91.6	93.6	8.2	0.02	0.17
VI0766_01	2008-05-26T03:05:07.274	25.0:45.0	23.3:0.3	93.8	96.3	7.0	0.03	0.24
VI0766_02	2008-05-26T03:19:07.289	45.0:70.0	23.5:2.1	92.8	94.2	6.8	0.02	0.11
VI0792_01	2008-06-21T03:37:10.343	25.0:40.0	2.3:3.1	98.0	100.7	8.3	0.07	0.67
VI0792_02	2008-06-21T03:50:10.343	45.0:70.0	2.3:4.7	93.5	95.0	7.5	0.03	0.25
VI0796_02	2008-06-25T03:42:10.367	25.0:40.0	2.8:3.6	91.3	94.7	8.7	0.01	0.10
VI0796_03	2008-06-25T03:55:10.371	45.0:70.0	2.7:5.2	91.2	94.0	7.6	0.01	0.09
VI0802_00	2008-07-01T03:32:44.307	10.0:20.0	20.1:20.8	92.5	95.0	9.0	0.06	0.55
VI0802_01	2008-07-01T03:49:44.389	25.0:40.0	20.5:21.3	94.7	96.3	6.0	0.05	0.37
VI0802_02	2008-07-01T04:03:44.411	45.0:65.0	18.9:21.3	98.8	99.8	4.3	0.16	0.74
VI0806_01	2008-07-05T03:54:48.428	25.0:40.0	20.9:21.8	96.3	98.3	9.3	0.10	0.98
VI0806_02	2008-07-05T04:08:48.562	45.0:70.0	19.5:21.8	95.6	96.8	4.6	0.04	0.26

Table 1. (continued)

					Volume Emission Rate			
Limb Session	Start Time	Latitude Range (deg)	Local Time Range (h)	Peak From Limb (km)	Peak (km)	FWHM (km)	Peak Intensity (MR/km)	Total VER (MR)
VI0843_03	2008-08-11T05:19:18.518	25.0:45.0	1.3:2.0	93.5	95.3	6.3	0.03	0.23
VI0847_03	2008-08-15T05:28:28.552	25.0:45.0	1.8:2.4	94.3	97.0	7.0	0.06	0.45
VI0320_05	2007-03-07T06:37:36.350	60.0:70.0	0.4:7.3		Limb profile with double peak			
VI0321_04	2007-03-08T06:22:48.431	35.0:45.0	0.1:0.9		Limb profile with double peak			
VI0323_06	2007-03-10T06:07:10.379	20.0:30.0	0.5:1.4		Limb profile with double peak			
Nadir Session	Start Time	Latitude Range (deg)	Local Time Range (h)		Exposure Time (s)			
VI0044_01	2006-06-03T15:06:56.666	−79.4:−9.9	19.4:2.7		3.3			
VI0093_00	2006-07-22T15:00:09.328	−59.1:−2.5	1.3:4.7		3.3			
VI0093_01	2006-07-22T15:28:09.283	−60.9:7.3	20.9:1.5		3.3			
VI0093_02	2006-07-22T15:56:09.355	−45.2:11.3	19.3:22.8		3.3			
VI0264_04	2007-01-09T20:36:56.857	−78.6:−10.6	19.6:3.1		3.3			
VI0344_01	2007-03-30T23:32:32.734	−66.2:−9.3	19.6:23.7		18.0			
VI0574_05	2007-11-15T18:42:55.387	−40.1:15.7	21.5:0.4		8.0			
VI0586_01	2007-11-27T16:53:15.434	−62.3:8.6	21.6:2.6		8.0			

[a]List of the selected data in limb and nadir mode and some measured parameters. The session name is shown. The first two letters of the session name (VI) are fixed and they mean "Virtis Infrared"; the four numbers after VI are the orbit number; the two suffix numbers after the underscore are the session number, which is the progressive observation number within the considered orbit. The start time of the acquisition is shown. Each limb observation lasts typically 30–40 min. The range of latitude spanned by the considered observation is given. The local time spanned range by the considered observation is given. The observed peak altitude for the limb profile, averaged over the latitude range of the session, is given (only limb mode). The parameters from the retrieved volume emission rate are the peak altitude, the FWHM, the peak intensity, and the integrated volume emission rate along the perpendicular direction. All the parameters reported are an average of all the grid point values within the range of latitude of each session. For the peak altitudes and the FWHM, an accuracy of ±1 km can be assumed. For the peak intensity and VER, an accuracy of ±10% can be assumed. The exposure time for all the limb observations is 8.0 s.

[b]Used to infer the ratio 1.27 μm/1.58 μm. The ratio is calculated from a portion of the session where the intensity is brighter and not from the full session. For nadir data, the exposure time is 3.3, 8.0, or 18.0 s.

Figure 2b. Figure 2 includes limb profiles from the sessions shown in Figures 1a and 1b (sessions 76_18 and 271_09).

[13] In nadir mode observations, the thermal emission cannot be neglected so it must be removed from the observed radiance to quantify the oxygen nightglow emission. Our first step in determining the thermal emission was to construct a false color composite red-green-blue (RGB) image using data from the 1.285 (red), 1.275 (green), and 1.265 (blue) μm wavelengths, as shown in Figure 1c. Regions dominated by nightglow emission appear blue or white. Those dominated by thermal emission are pink or red. To quantitatively remove the thermal contribution at 1.27 μm, we have scaled the 1.18-μm radiance by an empirical factor ranging from 0.27 to 0.38. This empirical scaling factor was determined by selecting spectra with a small intensity at 1.265 μm and a high correlation between the radiances at 1.18 and 1.285 μm (reddish areas without O_2 emission on the RGB images). Variations in the scaling factor across the disk are due mostly to topography but there is a weak dependence on cloud structure.

[14] The scaling factor to remove the thermal contribution at 1.27 μm also has been estimated using radiative transfer model calculations. Synthetic spectra were calculated using a surface temperature of 735 K and the typical cloud structures found at middle to low latitudes [*Zasova et al.*, 2007]. The total vertical cloud opacity at 1.18 μm was varied from 20 to 50 by varying the opacity of each layer without altering the structure of the clouds, which were assumed to be composed of mode 1 and mode 2 particles with scale height of 4 km. The calculations used the ARS code [*Ignatiev et al.*, 2005], which is based on DISORT [*Stamnes et al.*, 1988], with 48 streams and the HITEMP database [*Pollack et al.*, 1993] for CO_2 absorption. For the synthetic spectra, the ratio of the integrated emission in the 1.27- and 1.18-μm windows, r = I(1.27)/I(1.18), is in the range from 0.28 to 0.34, consistent with the empirical ratio from 0.27 to 0.38. The ratio depends only weakly on the total vertical cloud opacity because the single scattering albedo of the particles is very high (0.99999 at 1.18 μm). The single scattering albedo in the 1.74-μm window is smaller, 0.99978, so it does not work as well for the thermal correction. The ratio is most sensitive to the surface temperature. If the surface temperature is changed by 15 K, which is equivalent to a 2 km change in surface altitude, then the ratio changes by 0.03 for a cloud opacity of 30.

[15] Vertical profiles of the volume emission rate are retrieved from the observed limb profiles using an onion peeling technique [*Sharma et al.*, 1988]. Figure 3 shows the vertical profile of the volume emission rate of the (0–0) oxygen nightglow retrieved for orbit 317_06. The emission rate is expressed in MR/km (or 10^7 photons cm^{-3}). The technique assumes the atmosphere is spherically symmetric, including the airglow emission layer. Nadir-view images, however, indicate the nightglow emission is spatially inhomogeneous. The effective consequence of our assumption of spherical symmetry is to distribute the nightglow emission observed at higher altitudes over a larger region than may be true in reality. As a result, the retrieved emission at lower altitudes is underestimated. Clear evidence for this is found when the retrieved intensity below the peak altitude becomes negative. For several orbits where the spherical symmetry assumption led to negative values for the retrieved nightglow emission below 90 km, we imposed

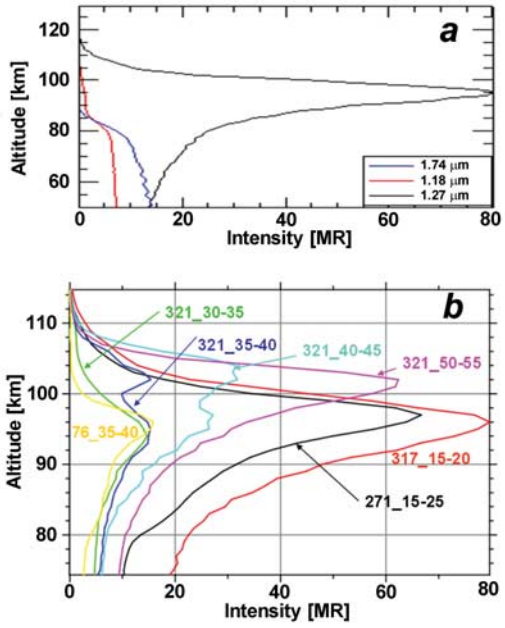

Figure 2. Limb profiles distribution of the O_2 (0–0) nightglow at 1.27 μm. (a) Limb profiles of radiance at 1.18 and 1.74 μm, shown in comparison with the O_2 (0–0) limb profile at 1.27 μm. The radiance at 1.18 and 1.74 μm is due to the scattered thermal emission from the deep atmosphere scattered to VIRTIS-M by the upper haze particles. Both radiances decay rapidly in the transition region of the upper boundary of the aerosol at about 90 km altitude. The thermal contribution at 1.27 μm should have a similar behavior; therefore, in the typical altitude range where the nightglow emitter resides (90–105 km), an almost pure nightglow emission is observed in limb view. (b) The first three numbers of the curve names are the number of the orbit, while the given range after the orbit number is the latitude range where the average was taken. Data from all local times spanned in the session were included in the average. One can see that the peak altitude emission and its brightness significantly vary from one orbit to the next one and even in the same orbit. From Figure 2, the profile seems wider in altitude at lower latitudes, and a double peak is often present with a peak at 96 and 103 km.

the additional constraint that the retrieved nightglow emission must be nonnegative. From these test cases, the upper limit on the geographic size of the emitting area was 500–1500 km, consistent with nadir images. When the retrieval is satisfactory, the shape of the vertical profile of the 1.27-μm radiance below 90 km coincides with that of the 1.18 μm-radiance, both providing the profile of thermal radiance from the deep atmosphere as scattered in the upper haze layer.

5. Vertical Distribution of the O_2(a-X) Nightglow Emission at 1.27 μm

[16] In Figure 4 we show observations from a single orbit of the (0–0) limb profiles averaged over 5° latitude intervals which were also averaged over the full local time span at each latitude, about 10–20 min; Figure 5 shows a selected

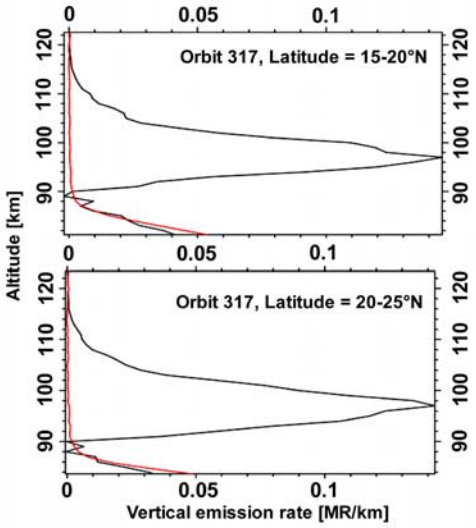

Figure 3. Vertical profiles of the O_2 (0–0) retrieved volume emission rate. Black curves are volume emission rate in O_2 (0–0) band at 1.27 μm, for orbit 317_06 in different latitude ranges; red curve is normalized radiance at 1.18 μm, which describes the upper boundary for the lower atmosphere thermal emission scattered into the VIRTIS-M field of view limb view. The normalized limb profile of thermal emission at 1.18 μm coincides well with the retrieved emission at 1.27 μm below 90 km, which is also thermal emission from the lower atmosphere.

set of limb observations from different orbits over a period of about 2 weeks (in contour plot style).

[17] These results reveal several characteristics of the O_2(a-X) nightglow emission. As was previously known, the intensity of the emission is highly variable. Figure 2b shows the maximum observed peak limb intensity varying from about 15 to 80 MR, and the minimum and maximum observed peak limb intensities in the 72 sessions studied are 4 and 100 MR, respectively. Figure 2b also demonstrates that the observed altitude of peak brightness can vary. This

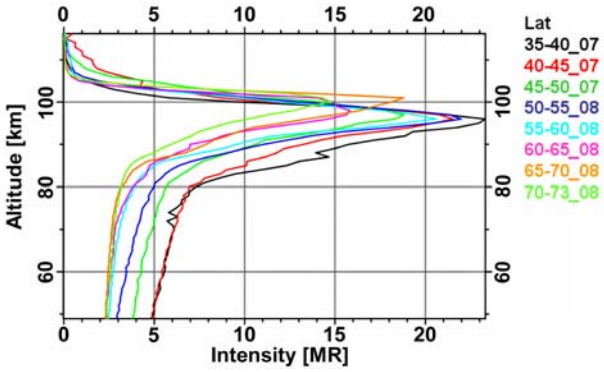

Figure 4. Limb profiles distribution of the O_2 (0–0) nightglow in limb mode. The intensity in limb view for orbit 317 at 35–73°N, session 7 and 8, is shown. Different peak altitudes are observed at different latitudes with a regular trend of correlation within this orbit. Also, the full width at half maximum (FWHM) appears wider toward the equator.

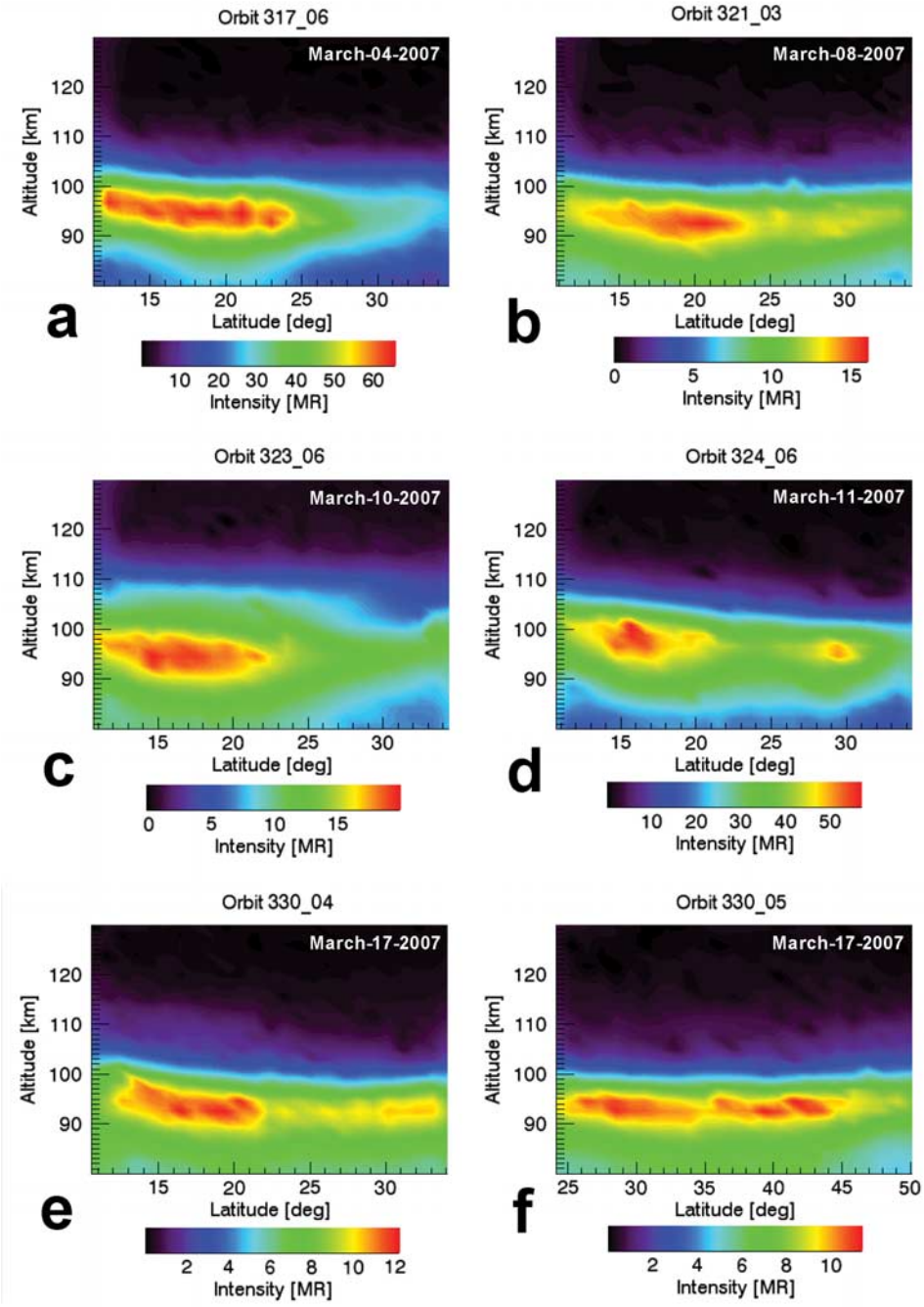

Figure 5. Limb profiles distribution of the O_2 (0–0) nightglow at 1.27 μm versus latitude. The intensity is integrated over all the local times at each latitude. The color bar is the intensity along the line of sight. The orbit and session number are given in the titles. The intensity can differ significantly from one limb observation to another, as, for example, in the case of Figures 5a and 5b. The altitude can be almost constant, like in Figure 5f, and moderately constant like in Figure 5c, or more frequently a slope is observed like in Figures 5d and 5e. Some small ''wave-like'' features, as in Figure 5b at 27°N, are real and may possibly be attributed to gravity waves.

is new information that cannot be obtained from nadir observations. In Figure 2b the observed peak altitude of the limb profile ranges from 96 to 103 km (for the higher peak of the double-peak profile), and the minimum and maximum altitudes for the observed peak of the nightglow limb profile in the 72 sessions studied are 90 and 102 km (for the single-peak profiles), respectively. Further study is required to assess whether the variations in the observed peak altitude may explain the temperature variations derived from ground-based observations of the emission [*Bailey et al.*, 2008]. Finally, significant variations have been detected in the shape of the observed limb profile (Figure 2b). Most

observed limb profiles have a single peak, as has been reported previously [*Drossart et al.*, 2007a; *Gérard et al.*, 2008], but some observed limb profiles have a double peak. This has not been reported previously and is discussed later in this paper.

[18] A view of the longer-term average characteristics of the (0–0) limb observations can be derived by using all of the limb data available in the VIRTIS data set to investigate the statistical characteristics of the retrieved vertical emission rate. The observed limb profile for each session, averaged over all local times (Table 1) was determined, assigned to a point on a 5° latitude range, and inverted to retrieve the vertical profile. Each retrieved vertical profile was then analyzed to derive the retrieved peak altitude, the peak altitude brightness, the FWHM of the retrieved vertical profile, and the total (column integrated) vertical emission rate. The mean values for each of these parameters for each latitude range are calculated and shown in Figure 6. Figure 6a shows the number of available limb observations for each latitude range. In Figure 6b, we show the meridional distribution of the mean peak altitude brightness. The abscissa is latitude, as for the other plots of Figure 6, and the ordinate is the intensity of the vertical emission rate at the retrieved peak altitude. The mean peak emission rate ranges from about 0.03 to 0.11 MR/km. Figure 6c shows the meridional distribution of the mean values of the altitudes at which the integrated line of sight (as observed, red curve) and vertical emission (as retrieved, blue curve) rates are maximum. For an ideally thin emitting layer, the observed peak altitude would coincide with the retrieved peak altitude. The observed peak altitude is systematically lower than the retrieved peak altitude by 2–3 km. Most of this bias is due to the geometrical effect of a not ideally thin emitting layer. In Figure 6d is shown the meridional distribution of the mean FWHM of the retrieved vertical profile of the oxygen nightglow. Figure 6e shows the total (column integrated) vertical emission rate, which, in turn, is equivalent to the intensity that would be seen in nadir view for pure oxygen nightglow emission. Finally, in Figure 6f, isolines of the mean total (column integrated) vertical emission rates are shown as a function of latitude and the retrieved peak altitude. The uncertainty in the peak altitudes and the FWHM is ±1 km, while that for the emission rate is ±10%. In all cases, however, the observed fluctuations are dominated by temporal variability in the nightglow emission. For this reason the error bar in the plots reports the standard deviation of this fluctuation.

[19] While the mean values discussed above represent the general morphology, there are occasional but significant deviations. For example in many cases the peak intensity decreases with increasing latitude, but sometimes it is observed an inverse behavior, as the one for example shown in Figure 2b, sessions 321_04 and 321_05. In some orbits of Figure 5, the maximum of the nightglow intensity is at subequatorial latitudes but there are secondary local maxima at higher latitudes. For example, session 324_06 (Figure 5d) has one maximum near 30°N and orbit 330 (Figures 5e and 5f) has several maxima at 25–45°N. Figure 5 also suggests an episodic variation in the maximum nightglow intensity with time for the region that was observed. The maximum intensity decreased by a factor of 4 over four days from session 317_06 (Figure 5a) to session 321_03 (Figure 5b) with almost the same local time; increased over the next three days, so that the observed maximum intensity in session 324_06 (Figure 5d) is similar to that in session 317_06; and then decreased again in session 330_04 (Figure 5e) to values similar to those observed in session 323_06 (Figure 5c). Some dynamical factors, such as breaking gravity waves at a local scale and tides at larger scales may disrupt the general picture, so long-term averages may reveal different dynamical information than the single orbit snapshots.

[20] The spatial distribution of the nightglow intensity derived from limb observations (Figure 6) is consistent with that found from the previous analysis of VIRTIS' nadir observations [*Gérard et al.*, 2008] and our analysis of a more complete set of nadir observations, as discussed later. In general, there is a negative correlation between the intensity of the emission and latitude. As shown in Figure 6b, the most intense emission observed is found at low latitudes. The peak altitude and the FWHM of the nightglow's vertical profile also show regular trends with latitude. As shown in Figure 6c, the mean retrieved peak altitude is highest at 45–50°N with a value of about 99 km, and appears to be relatively constant equatorward with a value of 97–98 km, while it decreases poleward with a relative minimum of 95 km at 65–70°N. The vertical FWHM of the emission shows a clearer trend, increasing from high to low latitudes with the largest FWHM, 11 km, at 5–10°N and the smallest, 6 km, at 60–65°N (see Figure 6d). The decrease of the observed peak altitude and its larger deviation (to lower altitudes) from the retrieved peak altitude toward the equator, see Figure 6c (left), can be explained by the increase of the vertical FWHM in this region. The thicker the emitting layer, the larger the difference between the observed and retrieved peak altitudes. A similar trend is found in Figure 4, where the observed peak altitude of the nested profiles increases with latitude, while FWHM and intensity decrease. The decrease in the peak altitude poleward of 45°N (Figure 6c) may indicate a different dynamical regime exists at the altitude of the emitting layer. This may be related to the influence of the polar vortex.

[21] Regions of intense nightglow where the peak altitude is approximately constant are likely to be regions of convergence for the subsolar to antisolar flow with strong downwelling. In terms of pressure, a constant peak altitude is consistent with the conditions to have very low horizontal pressure gradient forces which will suppress horizontal flow and give predominantly vertical flow. This is illustrated by the distribution of the total (column integrated) vertical emission rates derived from our limb observations (Figure 6e) and the distribution of peak altitudes (Figure 6c). The former increases by a factor of 6 from about 0.2 MR at 60–70°N to about 1.2 MR near the equator. The latter is relatively constant equatorward of 45°N. The overall picture derived from our limb observations is consistent with that derived from our own and previous analyses of nadir observations. In addition, we have been able to determine that the enhanced total (column integrated) vertical emission rate near the equator is due to both a more intense vertical emission rate at the retrieved peak altitude (Figure 6b) and a larger vertical FWHM for the emitting layer (Figure 6d). The former contributes a factor of three to the equatorial enhancement and the latter a factor of two. Finally, as shown in Figure 6f, the most intense O_2 nightglow emission is

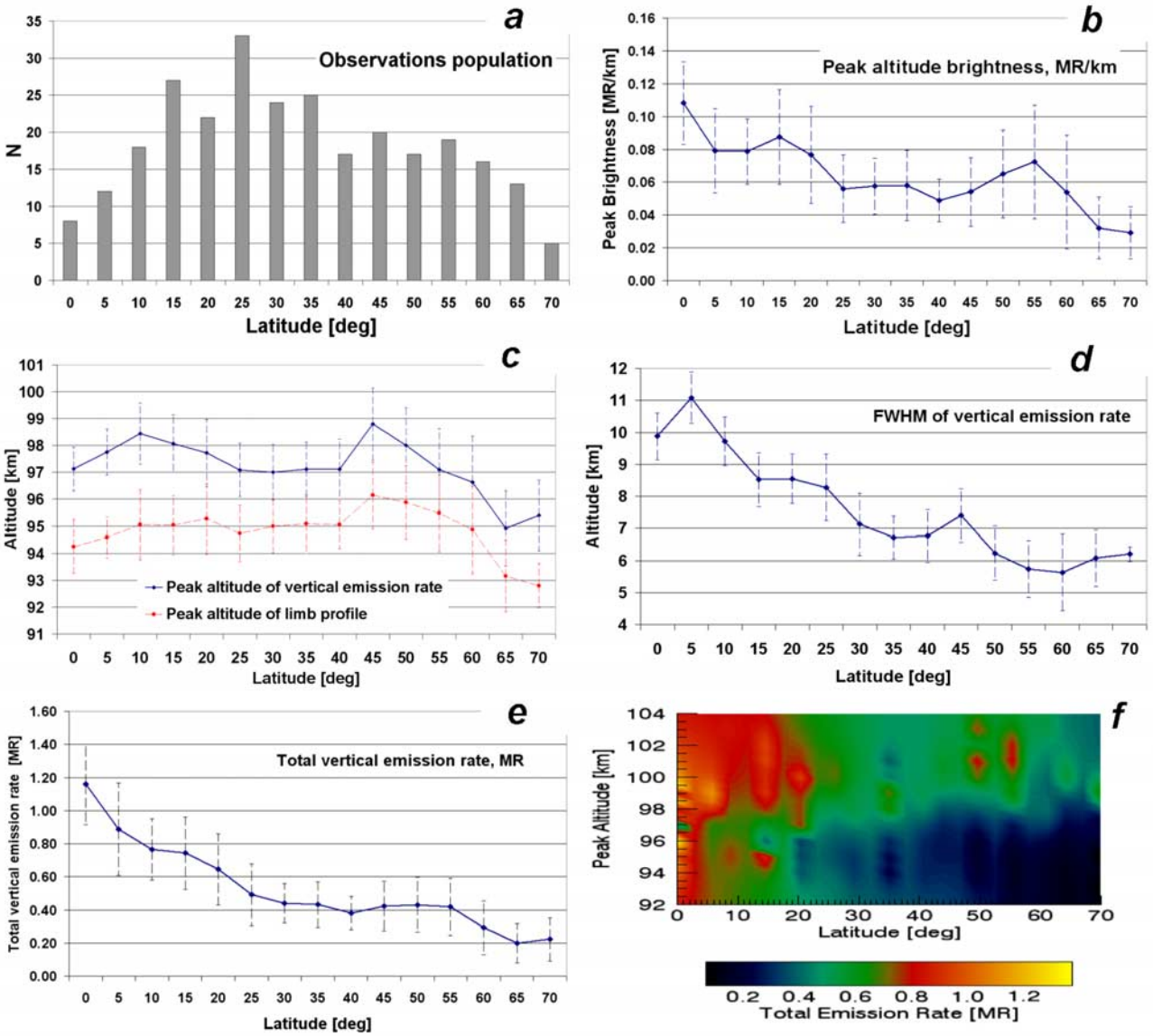

Figure 6. Mean vertical profile distribution of the O_2 (0–0) nightglow at 1.27 μm. (a) Number of available sessions in the latitude range is shown to indicate the number of samples over which the average is calculated for each latitude range. (b) Mean emission rate at peak altitude as a function of latitude. The error bar is the standard deviation. The maximum is found in the equatorial region, and the intensity decreases poleward. (c) Mean peak altitude of the volume emission rate (blue curve) and in limb profile (red curve) as a function of latitude. The error bar is the standard deviation. Figure 6 indicates the peak altitude of the volume emission is relatively constant and tends to decrease poleward of 45–50°N. The weak decrease of the peak altitude of the limb profile (red curve) is likely related to the wider FWHM at low latitudes. (d) Mean FWHM of the vertical profile as a function of latitude. The error bar is the standard deviation. The results show the FWHM is largest at low latitudes and decreases poleward with some relative peak at 45–50° and 70°N. (e) Mean total integrated vertical emission rate as a function of latitude. The error bar is the standard deviation. The maximum is found in the equatorial region, and the intensity decreases poleward. The slope is less pronounced than in Figure 6b owing to the amplification factor of Figure 6d. (f) Same as Figure 6e but as a function of latitude and peak altitude of the vertical profile. An uncertainty of ±10% in emission can be assumed. The intensity is highest at low latitudes when the peak altitude is higher.

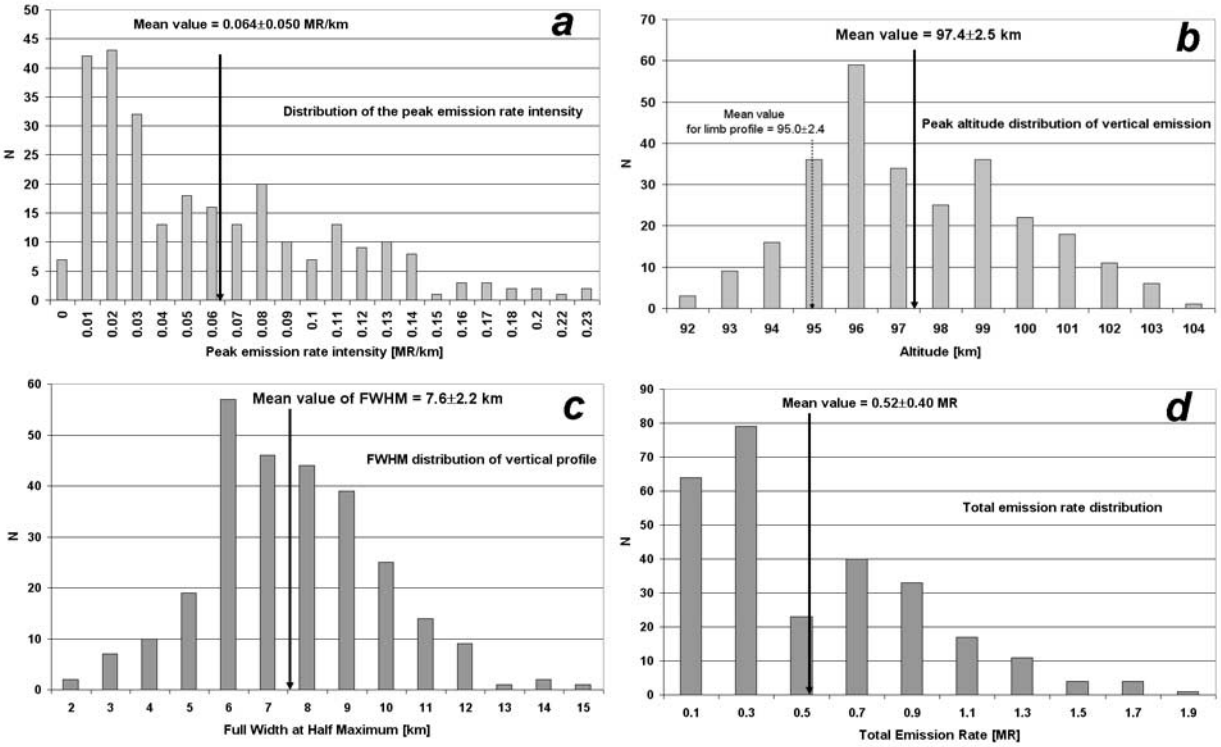

Figure 7. Population distribution of the oxygen nightglow parameters. (a) Distribution of the peak altitude emission rate intensity, same parameter as Figure 6b. It is remarkable the large variability of the intensity which is spread over a wide range of emission. The global mean value of the peak emission rate intensity is 0.064 ± 0.050 MR/km. (b) Distribution of the peak altitude of the vertical profile. Variability is less pronounced than in Figure 7a, and the global mean value of the peak altitude of emission is 97.4 ± 2.5 km. (c) Distribution of the FWHM of the vertical profile. The global mean value of FWHM is 7.6 ± 2.2 km. (d) Distribution of the total integrated vertical emission rate. Also, in this case the large variability is noticeable. The global mean value of the integrated emission rate is 0.52 ± 0.40 MR.

observed at near equatorial latitudes when the retrieved peak altitude is at least 98 km. These are the most favorable conditions for radiative deexcitation as opposed to collisional quenching.

[22] The statistical distributions of the parameters are shown in Figure 7. In average, the peak vertical emission rate intensity (peak altitude brightness) is 0.064 ± 0.050 MR/km (Figure 7a); the retrieved peak altitude is 97.4 ± 2.5 km and the observed peak altitude is 95.0 ± 2.4 km (Figure 7b); the vertical FWHM is 7.6 ± 2.2 km (Figure 7c); the total (column integrated) vertical emission rate is 0.52 ± 0.40 MR (Figure 7d). The observed and retrieved peak altitudes vary by ±2.5% across the range of latitudes observed while the total (column integrated) vertical emission rate varies by more than ±75%. A factor of 50 has been inferred from the limb to the perpendicular direction views of the intensity of the emitting layer in average.

6. Detection of Double-Peaked Nightglow

[23] In many cases two emission peaks are found in the observed limb profiles. Some examples are shown in Figures 2 and 8. In Figure 8a the measured limb profiles are shown on the left and the corresponding limb images at 1.27 μm on the right. The separation of the two layers is clear. On the occasions when a double peak is detected, the lower and higher peaks occur typically at 96–98 and 103–105 km, respectively, see Figure 8a and Figure 8b (left) where the retrieved vertical profiles are shown. Double peaks are more likely to occur at high latitudes, 45–70°N, although there are also occasional examples at lower latitudes. The higher peak is often the more intense of the two.

[24] The origin of the double peak is not yet understood. However, some suggestions can be provided. Given the uneven global distribution of the nightglow, one may think that the higher and lower peaks are the results of probing two separate emitting layers, each at a different altitude level. If so, the double peak would be a consequence of the viewing geometry. It is also possible the viewing geometry could produce an apparent double peak if both emitting regions are at the same radial distance from Venus but with a gap between them where there is less nightglow emission. Supposing this to be true for the case shown in Figure 8a, for the session 320_05, let's assume the higher peak as coming from a single-peaked layer located in a region at the LOS tangent altitude. The lower peak might be explained then with a local maximum of another emitting region placed off by 3° (about 310 km) from the former and at the same radial distance. However, this region of local maximum, estimated from the black curve of Figure 8a to

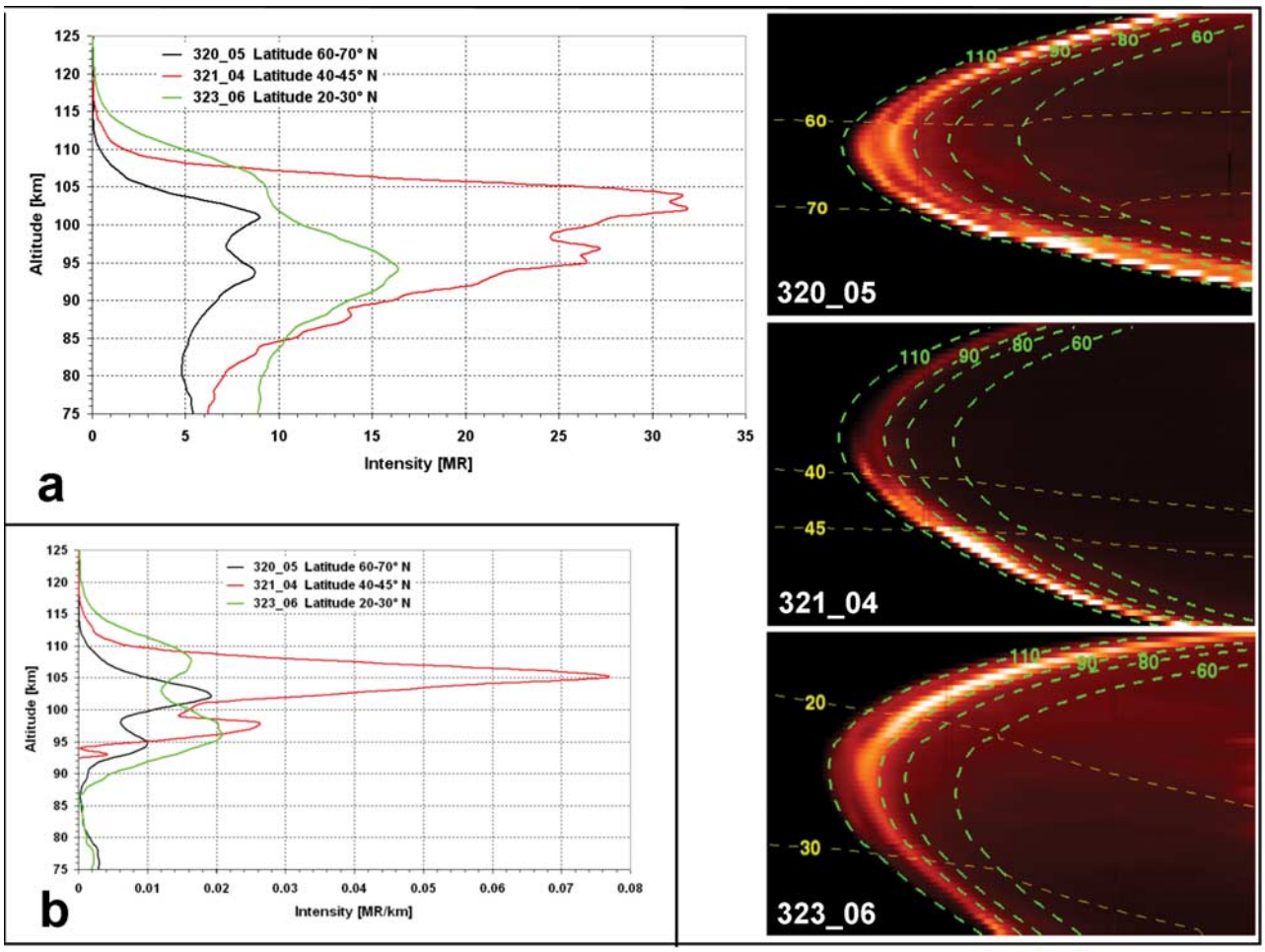

Figure 8. Profiles of the oxygen nightglow with double peak. (a) Comparison of different limb profiles for the (left) O_2 (0–0) nightglow at 1.27 μm and (right) the image view of the same observations. The green isolines in the images are the tangent altitude. The yellow isolines of the same images are latitudes, and they mark the latitudinal range where the limb profiles are taken. Color scale intensity is not the same for the images, in order to optimize the contrast. Double peaks are noticed in the limb profile on the left plots, and on the right, spatially separated layers can be seen in the acquired images. (b) Vertical emission rate retrieved for the profiles shown in Figure 8a. The double peak is observed also for the retrieved profiles and it results even more enhanced with relative peaks very well separated vertically.

be about 2.5 times brighter in total VER than the region responsible of the higher peak, should develop in a long strip precisely at this same distance for more than 20° latitude, corresponding to about 2000 km of spatial displacement (see Figure 8a, top right). Therefore, although these combinations can reproduce a double-peaked limb profile in some cases, this scenario appears to be very unlikely to explain the two distinct emitting layers of Figure 8 and several other similar observed cases not reported here.

[25] A third possible explanation, which is somewhat simpler and appears to be more likely than the other two, involves vertically propagating gravity waves. Gravity waves can modulate the conditions in the atmosphere, thereby modifying density, temperature, atomic oxygen abundance, and hence the collisional rate of recombining oxygen atoms and collisional quenching of the O_2(a) state. As a matter of fact, wave structures at Venus were observed by the Pioneer Venus Orbiter star trackers [*Bougher and Borucki*, 1994] in the same range of middle and high latitudes where double peaks are often found. Finally, it must be said that the retrieved atomic oxygen number density vertical profile is often double peaked even when the observed limb profile is single peaked [*Gérard et al.*, 2009].

7. O_2 Emission Rate From Nadir Observations

[26] Figure 9 shows a nadir-looking view of the nightglow. The emission rate has been corrected for thermal emission in the way described above, while emergence angle and cloud backscattering are corrected as was done by *Crisp et al.* [1996]. Various structures with clearly defined boundaries are visible in Figures 9a–9d that denote the complex interplay of dynamical and, possibly, chemical factors in the formation of the nightglow. Notwithstanding the significant variability observed, it seems that the distri-

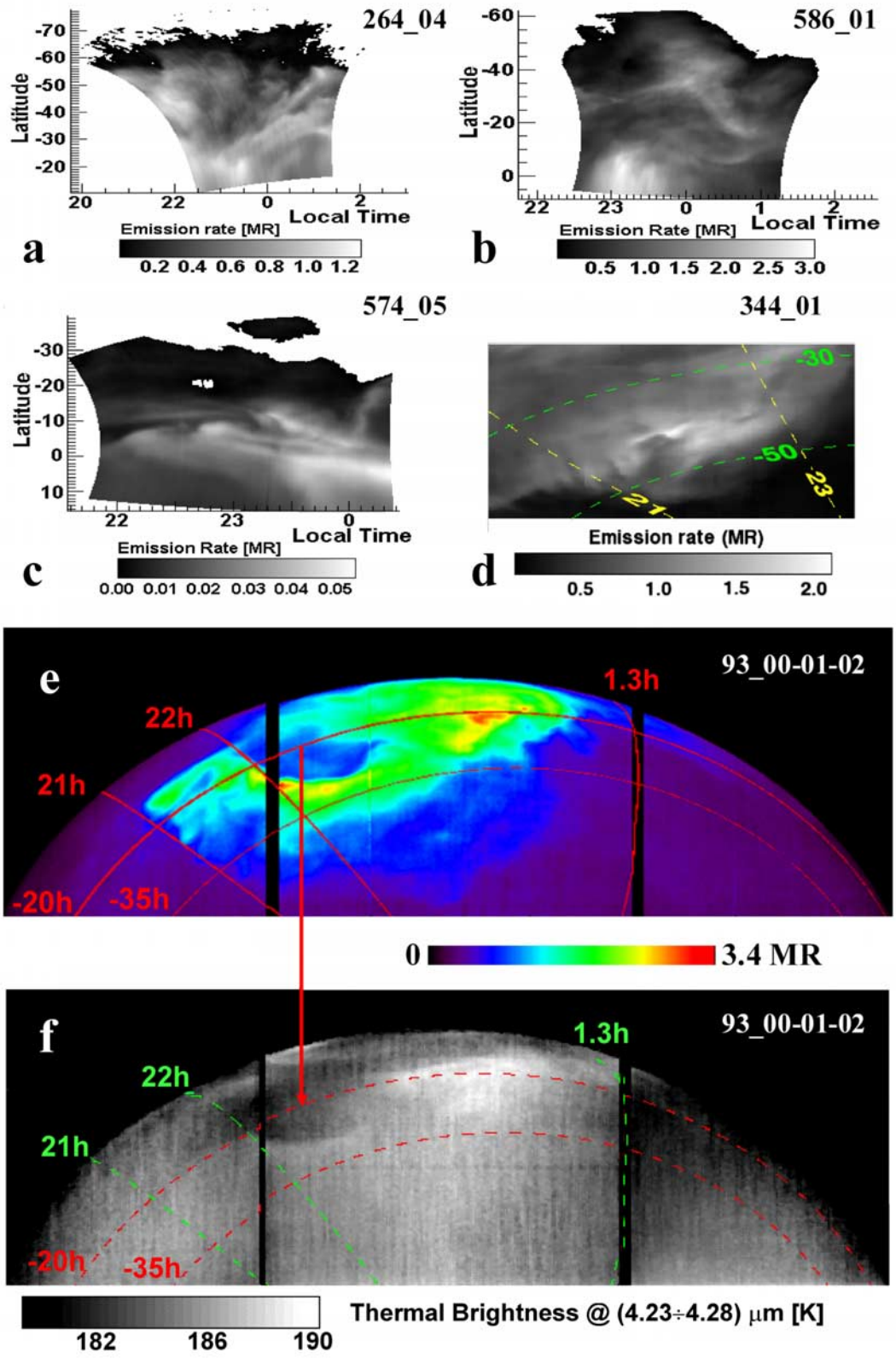
264_04
Latitude
-70
-60
-50
-40
-30
-20
20
22
0
2
Local Time
Emission rate [MR]
0.2 0.4 0.6 0.8 1.0 1.2
a
586_01
Latitude
-60
-40
-20
0
22
23
0
1
2
Local Time
Emission Rate [MR]
0.5 1.0 1.5 2.0 2.5 3.0
b
574_05
Latitude
-30
-20
-10
0
10
22
23
0
Local Time
Emission Rate [MR]
0.00 0.01 0.02 0.03 0.04 0.05
c
344_01
-30
-50
23
21
Emission rate (MR)
0.5 1.0 1.5 2.0
d
e
93_00-01-02
1.3h
22h
21h
-20h
-35h
0
3.4 MR
f
93_00-01-02
1.3h
22h
21h
-20h
-35h
182 186 190
Thermal Brightness @ (4.23÷4.28) μm [K]

Figure 9

bution of the nightglow over the planet is not entirely random but shows structured recurrent features. The emission patches may appear elongated, as seen in Figures 9a–9c, in the form of jets over extensions of 1700 to 2300 km, or as wavy features as in Figure 9d.

[27] We have searched for a connection between the nightglow and the local temperature. For this purpose, we have retrieved the average thermal brightness (TB) from the radiance in the 4.23–4.28 μm spectral interval which probes, according to radiative transfer models [*Grassi et al.*, 2008], the 90–93 km altitude range. Our approach is somewhat simpler than that used in the formal retrieval in that work, but the TB provides reliable relative values. In Figures 9e and 9f, intense nightglow seems to be correlated with elevated temperatures. Other authors have reported similar conclusions [*Ohtsuki et al.*, 2005, 2008; *Bailey et al.*, 2008; *Bertaux et al.*, 2007], and it has been suggested that the intense nightglow may be caused by strong downwelling and resulting compressional heating. Conversely, the dim nightglow regions, if affected by upwelling, may be involved in expansion cooling with consequently lower temperatures than the surrounding environment. The same effects may also be a consequence of the atmospheric temperature structure modulation induced by vertically propagating gravity waves. The circular dark region of faint nightglow has on average a local TB of 182 K, lower by about 3 K than the surroundings with a TB of 185 K. The TB may differ by a few K from the formally retrieved actual absolute atmospheric temperatures, but their relative accuracy is estimated to be better than 1 K, so these temperature differences are considered significant. The bright region at the top (Figure 9f) where TB is on average about 189 K, corresponds to the region in Figure 9e where the nightglow is brightest and therefore the downwelling is a maximum in this region.

[28] We have also performed a long-term study of the nightglow global distribution. For this purpose, a series of observations made with exposure times of at least 0.1 s and emergence angles smaller than 80° have been selected from 880 orbits. The radiances are subsequently corrected for thermal radiation (a constant factor of 0.3 was used in this case for scaling the 1.18 μm radiance), emission angle and cloud backscattering as previously discussed. The resulting image is shown in Figure 10a. The brightest region has a total (column integrated) vertical emission rate of 1.2 MR, consistent with the maximum derived from limb observations (Figure 6e). The center of the brightest region is about 5°S of the AS point, the proximity to which is an expected outcome of the subsolar to antisolar circulation. Figure 10b shows the map of coverage for the data used in Figure 10a, where the color scale bar represents the $\log_{10}$ of counts.

8. Oxygen Band Ratio

[29] The (0–1) band of the a-X system that occurs at 1.58 μm is weaker than the 1.27 μm band. It is the former, however, that was first observed in the terrestrial atmosphere in the evening twilight ground experiment by *Vallance Jones and Harrison* [1958]. The atmospheric transmission at 1.27 μm is significantly lower, making it difficult for photons at this wavelength to reach the Earth's surface. Some years would have to pass before the in-flight detection of the (0–0) band by *Noxon and Vallance Jones* [1962], and some more for *Lowe* [1969] to resolve it in a spectrum recorded from the ground. The nondetection of the (0–0) band in the pioneering work of *Vallance Jones and Harrison* [1958] was interpreted by the authors to mean a ratio of transition probabilities $A_{00}/A_{01} = 10$, which is the value still in place in the current version of the HITRAN database [*Rothman et al.*, 2005]. Observations of the (0–1) band in the terrestrial atmosphere continue, driven by the interest in investigating the oxygen chemistry of the mesosphere and lower thermosphere.

[30] There have been a few subsequent estimates of the ratio, that have come either from laboratory experiments, e.g., $A_{00}/A_{01} = 46.0 \pm 0.7$ [*Findlay*, 1969], 49.5 ± 4 [*Becker et al.*, 1971], 80 ± 20 [*Haslett and Fehsenfeld*, 1969], and 55 ± 10 [*Thomas and Thrush*, 1977]; or from airglow observations, some times in combination with photochemical modeling, e.g., $A_{00}/A_{01} = 52 \pm 25$ [*Winick et al.*, 1985], and 80 ± 15 [*Pick et al.*, 1971]. More recently, *Kassi et al.* [2005] have determined the line strengths of a few lines belonging to the strong Q branch in a high-resolution absorption spectrum experiment. By comparison to the respective lines in HITRAN, and after the correction of a numerical inconsistency in the conversion of absorption strengths to transition probabilities (confirmed by the authors), the work of *Kassi et al.* [2005] leads to $A_{00}/A_{01} = 55–60$. Recalling that on the basis of the Franck-Condon principle the predicted ratio is $A_{00}/A_{01} = 148$ [*Kassi et al.*, 2005] and that the principle is less likely to operate in long-lived states, it is important to note the fundamental interest that the discrepancy between theory and experiments bears.

[31] The VIRTIS instrument can resolve simultaneously the absolute radiances from both emission bands in the nighttime spectrum of Venus' upper atmosphere. This was utilized by *Piccioni et al.* [2008] to infer $A_{00}/A_{01} = 63 \pm 6$. We now provide the ratio from a more extended data set and also how the ratio was determined.

Figure 9. Observations of the oxygen nightglow in nadir view geometry. O_2 (0–0) nightglow observations at 1.27 μm, after thermal, emergence angle, and cloud backscattering corrections: (a) orbit 264, session 04; (b) orbit 586, session 01; (c) orbit 574, session 05; (d) orbit 344, session 01. The green and yellow isolines are latitude and local time, respectively. (e) Orbit 93, mosaic of session 00, 01, and 02. The isolines from left to right are local time while the others from top to bottom are latitude. (f) Thermal brightness of the same observation as in Figure 9e, averaged from 4.23 to 4.28 μm which probes, according to radiative transfer calculation, the 0.1 mbar pressure level, corresponding to about 90–93 km altitude. The green and red isolines are local time and latitude, respectively. The extension of the long stripes in Figure 9a is of the order of 1700–2300 km. The thermal brightness (TB) of the dark patch indicated by the arrow is about 182 K, which is 3 K lower than the surrounding. This is visibly correlated with the corresponding dark patch in Figure 9e of the oxygen nightglow. The diagonal dimension of the dark circular feature is about 800 km. The brighter region in the top middle of Figure 9e has the highest TB of the image, about 189 K, which is consistent with the maximum downwelling zone.

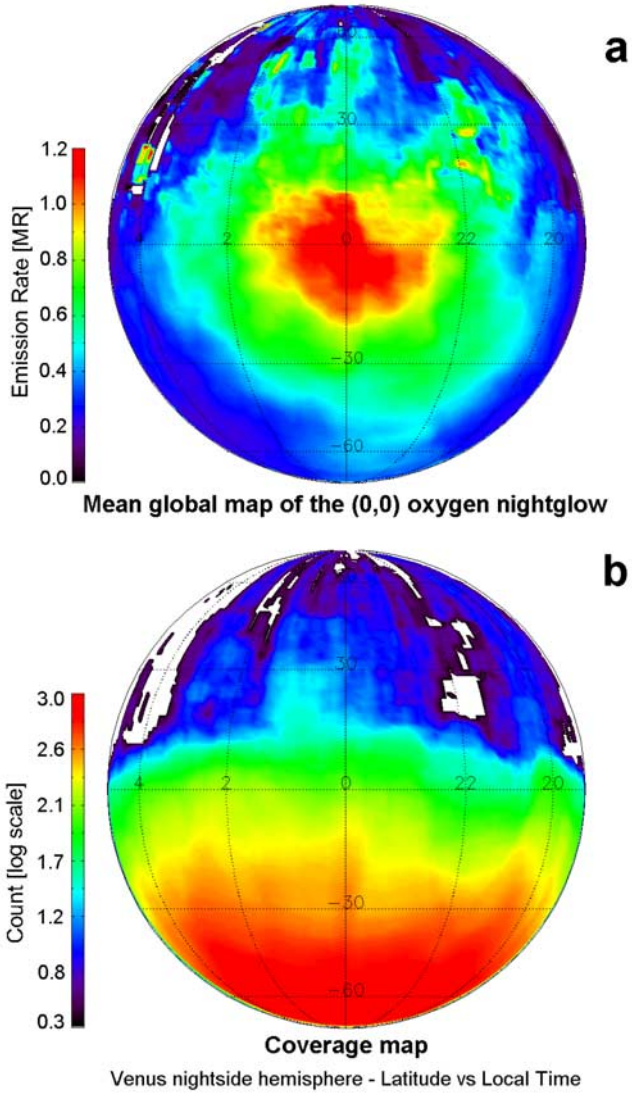

Figure 10. Global map of the oxygen nightglow over 880 orbits in nadir geometry. (a) Mean global O_2 (0–0) nightglow at 1.27 μm, after thermal, emergence angle, and cloud backscattering corrections, averaged over 880 orbits. The map is constructed with all the available nadir observations in nighttime with an exposure time greater or equal than 0.3 s. The region of maximum emission, 1.2 MR, is near the antisolar (AS) point, a clear indication of the subsolar (SS) to AS circulation, but with a slight shift of the patch center toward the morning sector, to about 0015, and south, to 5°S. (b) Counts of the coverage map for the same data set as Figure 10a. Color scale bar is $\log_{10}$ (counts). The geometry of the orbit permits more frequent observations of the southern polar region owing to the longer persistence and farther distance of the apocenter which is located approximately over the south pole. However, it is shown that even in the less covered portion in the equatorial region, hundreds of observations are present.

[32] For the analysis we have used portions of the 36 limb observations from Table 1 with relatively high intensity for the (0–0) band, of the order of 0.5 MR or greater, in the period March 2007 to January 2008. To avoid the contribution of the thermal emission scattered by the clouds and haze, only observations with tangent altitude in the 90–100 km range have been used. The continuum has been subtracted by linearly interpolating the observed radiances between 1.24 and 1.3 μm for the (0–0) band and 1.55 and 1.60 μm for the (0–1) band. At the relevant temperatures, no contribution from the oxygen nightglow is expected outside these intervals. Subsequently we integrated the radiances for each transition to obtain the total emission rate. In Figure 11a the observed limb profiles from session 317_06 of the (0–0) and (0–1) bands at 1.27 and 1.58 μm, respectively, are shown as an example. In Figure 11b the ratios of the integrated radiances are shown. The mean radiance ratio integrated over the selected altitude range of 90–100 km, and weighted by the inverse square of the uncertainty is 78 ± 10, which results in 63 ± 8 for the ratio of transition probabilities A_{00}/A_{01}. The uncertainty is largely due to the difficulty of evaluating the continuum of the 1.58-μm band so it is largest when the SNR in this spectral region is low.

9. Conclusions

[33] A study of Venusian molecular oxygen nightglow in the (0–0) and (0–1) bands at 1.27 and 1.58 μm, respectively, from limb and nadir geometry has been conducted with the VIRTIS instrument on board Venus Express. Limb geometry data in the period from July 2006 to August 2008 as well as some nadir data, acquired in the period from 3 June 2006 to 27 November 2007, have been shown, described, analyzed, and compared with the thermal brightness at 4.23 to 4.28 μm, which probes the 0.1 mbar level of pressure, corresponding to about 90–93 km altitude. All nadir data acquired in the period from 14 May 2006 to 14 September 2008, about 4 Venusian years, have been used to globally map the 1.27 μm emission averaged over this period of time (after correction for thermal emission, emergence angle and cloud backscattering).

[34] The shape and the intensity of the 1.27 μm vertical profile are highly variable, however some regularities have been identified. The mean distribution of the total (column integrated) vertical emission rate inferred from limb observations is consistent with that derived from nadir observations over a 2-year period with the most intense nightglow emission found near the antisolar region. The retrieved peak altitude is relatively independent of latitude equatorward of 45–50°N, with a mean value of 97.4 km while a different dynamical regime is identified poleward of this latitude. The vertical FWHM shows a significant increase with decreasing latitude and it reaches its maximum of 11 km in the equatorial region. The observed emission is most intense at low latitudes when the retrieved peak altitude is above 98 km. It has been shown that the intense total (column integrated) vertical emission rate that is observed near the antisolar point is due to both a more intense volume emission rate at the retrieved peak altitude and a thicker emitting layer. Limb profiles with two peaks have been observed. These could be related to vertically propagating gravity waves modulating the atmospheric structure.

[35] Significant variability in the instantaneous local distribution of 1.27 μm emission rate in nadir mode is found, however features frequently appear very well struc-

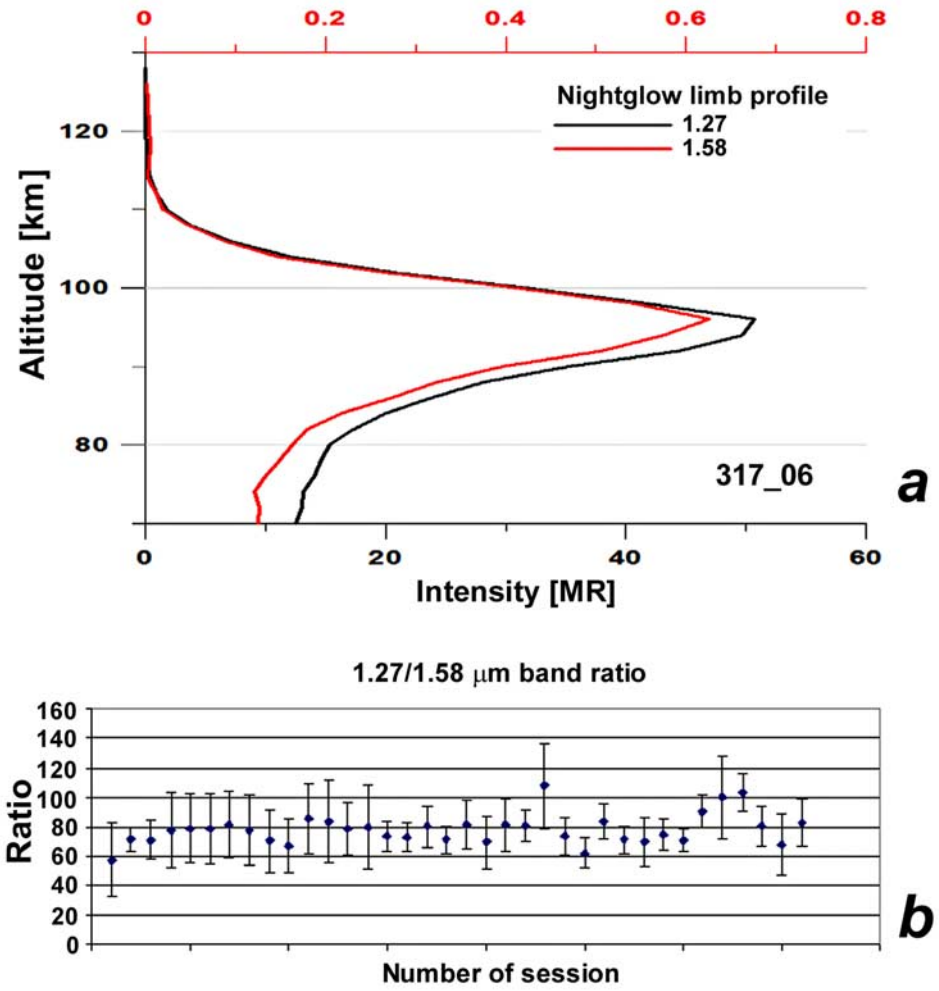

Figure 11. O_2 (0–0) and (0–1) limb profiles and radiance ratio. (a) Intensity of limb profiles for total integrated emission in the (0–0) and (0–1) O_2 transitions at 1.27 and 1.58 μm are shown for session 317_06. The intensity was averaged over the full range of latitude and local time of the session. The red scale shows the intensity value for the (0–1) transition, in MR. Their peak altitudes are in agreement. (b) O_2 (0–0) and (0–1) radiance ratio in limb mode at 1.27 and 1.58 μm is shown. The statistic takes in account all the data analyzed in the period March 2007 to January 2008 marked with a superscript "b" in Table 1. The ratio is calculated in a selected bright region of the session only and not over the full spanned latitude and local time range of the session. This is why there is no direct correspondence from the ratio calculated from Figure 11a and the relevant point of the session in Figure 11b. The weighted mean value of the radiance ratio is 78 ± 10, which translates into 63 ± 8 in terms of the ratio of the transition probabilities A_{00}/A_{01}.

tured, with very elongated bright stripes similar to jets and wavy type formations. A correlation of the nightglow intensity and the thermal brightness probed at the altitude of about 90–93 km is often found in the instantaneous snapshot. Dark circular shape features occur frequently in the nightglow map and usually have a thermal brightness that is lower than the surrounding bright nightglow region. This suggests these dark regions may be places at which upwelling flow has inhibited the recombination of oxygen atoms and produced localized cooling. These dark features could also be produced by vertically propagating gravity waves. Finally, both the (0–0) and (0–1) bands have been simultaneously measured in the VIRTIS spectra and a ratio of the transition probabilities A_{00}/A_{01} = 63 ± 8 has been inferred.

[36] **Acknowledgments.** We gratefully acknowledge the work of the entire VIRTIS and Venus Express teams that allowed these data to be obtained and discussed. We wish to thank ASI, CNES, and the other national space agencies that have supported this research. Russian coauthors acknowledge Russian Foundation of Basic Research for grant RFFI 08-02-00850. Partial funding for this research was provided by the Australian Research Council. Helpful comments from two anonymous reviewers, D. Titov and R. Carlson, are gratefully acknowledged.

References

Alexander, M. J. (1992), A mechanism for the Venus thermospheric superrotation, *Geophys. Res. Lett.*, *19*, 2207–2210, doi:10.1029/92GL02110.

Allen, D. A., and J. W. Crawford (1984), Cloud structure on the dark side of Venus, *Nature*, *307*, 222–224, doi:10.1038/307222a0.

Bailey, J., V. S. Meadows, S. Chamberlain, and D. Crisp (2008), The temperature of the Venus mesosphere from $O_2(a^1\Delta_g)$ airglow observations, *Icarus*, *197*, 247–259, doi:10.1016/j.icarus.2008.04.007.

Becker, K. H., W. Groth, and U. Schurath (1971), The ratio of the Franck-Condon factors q(0, 0)/q(0, 1) of the infrared atmospheric band system of

oxygen, *Planet. Space Sci.*, *19*, 1009–1010, doi:10.1016/0032-0633(71)90150-4.

Bertaux, J. L., et al. (2007), A warm layer in Venus' cryosphere and high altitude measurements of HF, HCl, H2O, and HDO, *Nature*, *450*, 646–649, doi:10.1038/nature05974.

Bougher, S. W., and W. J. Borucki (1994), Venus O_2 visible and IR nightglow: Implications for lower thermosphere dynamics and chemistry, *J. Geophys. Res.*, *99*, 3759–3776, doi:10.1029/93JE03431.

Bougher, S. W., S. Rafkin, and P. Drossart (2006), Dynamics of the Venus upper atmosphere: Outstanding problems and new constraints expected from Venus Express, *Planet. Space Sci.*, *54*, 1371–1380, doi:10.1016/j.pss.2006.04.023.

Cheah, S.-L., Y.-P. Lee, and J. F. Ogilvie (2000), Wavenumbers, strengths, widths, and shifts with pressure of lines in four bands of gaseous $^{16}O_2$ in the systems $a^1\Delta_g - X^3\Sigma_g^-$ and $b^1\Sigma_g^+ - X^3\Sigma_g^-$, *J. Quant. Spectrosc. Radiat. Transfer*, *64*, 467–482.

Connes, P., J. F. Noxon, W. A. Traub, and N. Carleton (1979), $O_2(a^1\Delta_g)$ emission in the day and night airglow of Venus, *Astrophys. J.*, *233*, L29–L32, doi:10.1086/183070.

Crisp, D., V. S. Meadows, B. Bézard, C. de Bergh, J.-P. Maillard, and F. P. Mills (1996), Ground-based near-infrared observations of the Venus nightside: 1.27 μm $O_2(a^1\Delta_g)$ airglow from the upper atmosphere, *J. Geophys. Res.*, *101*, 4577–4594, doi:10.1029/95JE03136.

Drossart, P., et al. (2007a), A dynamic upper atmosphere of Venus as revealed by VIRTIS on Venus Express, *Nature*, *450*, 641–645, doi:10.1038/nature06140.

Drossart, P., et al. (2007b), Scientific goals for the observation of Venus by VIRTIS on ESA/Venus express mission, *Planet. Space Sci.*, *55*, 1653–1672, doi:10.1016/j.pss.2007.01.003.

Findlay, F. D. (1969), Relative band intensities in the atmospheric and infrared atmospheric systems of molecular oxygen, *Can. J. Phys.*, *47*, 687–691.

Gamache, R. R., and A. Goldman (2001), Einstein A coefficient, integrated band intensity, and population factors: Application to the $a^1\Delta_g - X^3\Sigma_g^-$ (0, 0) O_2 band, *J. Quant. Spectrosc. Radiat. Transfer*, *69*, 389–401, doi:10.1016/S0022-4073(00)00072-8.

Gérard, J.-C., A. Saglam, G. Piccioni, P. Drossart, C. Cox, S. Erard, R. Hueso, and A. Sánchez-Lavega (2008), Distribution of the O_2 infrared nightglow observed with VIRTIS on board Venus Express, *Geophys. Res. Lett.*, *35*, L02207, doi:10.1029/2007GL032021.

Gérard, J.-C., A. Saglam, G. Piccioni, P. Drossart, F. Montmessin, and J.-L. Bertaux (2009), Atomic oxygen distribution in the Venus mesosphere from observations of O_2 infrared airglow by VIRTIS-Venus Express, *Icarus*, *199*, 264–272, doi:10.1016/j.pss.2006.04.023.

Gierasch, P. J., et al. (1997), The general circulation of the Venus atmosphere: An assesment, in *Venus II: Geology, Geophysics, Atmosphere, and Solar Wind Environment*, edited by S. W. Bougher et al., pp. 459–500, Univ. of Ariz. Press, Tucson.

Grassi, D., P. Drossart, G. Piccioni, N. I. Ignatiev, L. V. Zasova, A. Adriani, M. L. Moriconi, P. G. J. Irwin, A. Negrão, and A. Migliorini (2008), Retrieval of air temperature profiles in the Venusian mesosphere from VIRTIS-M data: Description and validation of algorithms, *J. Geophys. Res.*, *113*, E00B09, doi:10.1029/2008JE003075.

Haslett, J. C., and F. C. Fehsenfeld (1969), Ratio of the $O_2(a^1\Delta_g - X^3\Sigma_g^-)$ (0, 0), (0, 1) transitions, *J. Geophys. Res.*, *74*, 1878–1879, doi:10.1029/JA074i007p01878.

Hueso, R., A. Sánchez-Lavega, G. Piccioni, P. Drossart, J. C. Gérard, I. Khatuntsev, L. Zasova, and A. Migliorini (2008), Morphology and dynamics of Venus oxygen airglow from Venus Express/Visible and Infrared Thermal Imaging Spectrometer observations, *J. Geophys. Res.*, *113*, E00B02, doi:10.1029/2008JE003081.

Huestis, D. L. (2002), Current laboratory experiments for planetary aeronomy, in *Atmospheres in the Solar System: Comparative Aeronomy*, *Geophys. Monogr. Ser.*, vol. 130, edited by M. Mendillo, A. Nagy, and J. H. Waite, pp. 245–258, AGU, Washington, D. C.

Ignatiev, N. I., D. Grassi, and L. V. Zasova (2005), Planetary Fourier Spectrometer data analysis: Fast radiative transfer models, *Planet. Space Sci.*, *53*, 1035–1042, doi:10.1016/j.pss.2004.12.009.

Kamp, L. W., F. W. Taylor, and S. B. Calcutt (1988), Structure of Venus's atmosphere from modelling of night-side infrared spectra, *Nature*, *336*, 360–362, doi:10.1038/336360a0.

Kassi, S., D. Romanini, and A. Campargue (2005), Very high sensitivity CW-cavity ring down spectroscopy: Application to the $a^1\Delta_g(0) - X^3\Sigma_g^-(1)$ O_2 band near 1.58 μm, *Chem. Phys. Lett.*, *409*, 281–287, doi:10.1016/j.cplett.2005.05.033.

Lafferty, W. J., A. M. Solodov, C. L. Lugez, and G. T. Fraser (1998), Rotational line strengths and self-pressure-broadening coefficients for the 1.27-μm, $a^1\Delta_g - X^3\Sigma_g^-$, v = 0–0 band of O_2, *Appl. Opt.*, *37*, 2264–2270, doi:10.1364/AO.37.002264.

Lellouch, E., T. Clancy, D. Crisp, A. J. Kliore, D. Titov, and S. W. Bougher (1997), Monitoring of mesospheric structure and dynamics, in *Venus II: Geology, Geophysics, Atmosphere, and Solar Wind Environment*, edited by S. W. Bougher et al., pp. 295–324, Univ. of Ariz. Press, Tucson.

Limaye, S. S. (2007), Venus atmospheric circulation: Known and unknown, *J. Geophys. Res.*, *112*, E04S09, doi:10.1029/2006JE002814.

Lowe, R. P. (1969), Interferometric spectra of the Earth's airglow (1.2–1.6 μm), *Philos. Trans. R. Soc. London, Ser. A.*, *264*, 163–169.

Markiewicz, W. J., D. V. Titov, S. S. Limaye, H. U. Keller, N. Ignatiev, R. Jaumann, N. Thomas, H. Michalik, R. Moissl, and P. Russo (2007), Morphology and dynamics of the upper cloud layer of Venus, *Nature*, *450*, 633–636, doi:10.1038/nature06320.

Meadows, V. S., and D. Crisp (1996), Ground-based near-infrared observations of the Venus nightside: The thermal structure and water abundance near the surface, *J. Geophys. Res.*, *101*, 4595–4622, doi:10.1029/95JE03567.

Miller, H. C., J. E. McCord, J. Choy, and G. D. Hager (2001), Measurement of the radiative lifetime of $O_2(a^1\Delta_g)$ using cavity ring down spectroscopy, *J. Quant. Spectrosc. Radiat. Transfer*, *69*, 305–325.

Mills, F. P., and M. Allen (2007), A review of selected issues concerning the chemistry in Venus' middle atmosphere, *Planet. Space Sci.*, *55*, 1729–1740, doi:10.1016/j.pss.2007.01.012.

Newman, S. M., I. C. Lane, A. J. Orr-Ewing, D. A. Newnham, and J. Ballard (1999), Integrated absorption intensity and Einstein coefficients for the O_2 $a^1\Delta_g - X^3\Sigma_g^-$ (0, 0) transition: A comparison of cavity ringdown and high resolution Fourier transform spectroscopy with a long-path absorption cell, *J. Chem. Phys.*, *110*, 10,749–10,757, doi:10.1063/1.479018.

Noxon, J. F., and A. Vallance Jones (1962), Observation of the (0, 0) band of the $(a^1\Delta_g - X^3\Sigma_g^-)$ system of oxygen in the day and twilight airglow, *Nature*, *196*, 157–158, doi:10.1038/196157a0.

Ohtsuki, S., N. Iwagami, H. Sagawa, H. Kasaba, Y. Ueno, and M. Imamura (2005), Ground-based observation of the Venus 1.27-μm O_2 airglow, *Adv. Space Res.*, *36*, 2038–2042, doi:10.1016/j.asr.2005.05.078.

Ohtsuki, S., et al. (2008), Imaging spectroscopy of the Venus 1.27-μm O_2 airglow with ground-based telescopes, *Adv. Space Res.*, *41*, 1375–1380, doi:10.1016/j.asr.2007.10.014.

Piccioni, G., et al. (2008), First detection of hydroxyl in the atmosphere of Venus, *Astron. Astrophys.*, *483*, L29–L33, doi:10.1051/0004-6361:200809761.

Piccioni, G., et al. (2009), VIRTIS: The Visible and Infrared Thermal Imaging Spectrometer, *Eur. Space Agency Spec. Publ.*, *ESA SP-1295*, in press.

Pick, D. R., E. J. Llewellyn, and A. Vallance Jones (1971), Twilight airglow measurements of the OH and O2 bands by means of balloon-borne instruments, *Can. J. Phys.*, *49*, 897–905.

Pollack, J. B., et al. (1993), Near-infrared light from Venus' nightside: A spectroscopic analysis, *Icarus*, *103*, 1–42, doi:10.1006/icar.1993.1055.

Rothman, L. S., et al. (2005), The HITRAN 2004 molecular spectroscopic database, *J. Quant. Spectrosc. Radiat. Transfer*, *96*, 139–204, doi:10.1016/j.jqsrt.2004.10.008.

Sánchez-Lavega, A., et al. (2008), Variable winds on Venus mapped in three dimensions, *Geophys. Res. Lett.*, *35*, L13204, doi:10.1029/2008GL033817.

Sander, S. P., et al. (2006), Chemical kinetics and photochemical data for use in atmospheric studies evaluation number 15, *JPL Publ.*, *06-2*, 523 pp.

Sharma, R. D., H. B. Harlow, and J. P. Riehl (1988), Determination of atomic oxygen density and temperature of the thermosphere by remote sensing, *Planet. Space Sci.*, *36*, 531–538, doi:10.1016/0032-0633(88)90022-0.

Slanger, T. G., and R. A. Copeland (2003), Energetic oxygen in the upper atmosphere and the laboratory, *Chem. Rev.*, *103*, 4731–4765, doi:10.1021/cr0205311.

Spalek, O., J. Kodymová, P. Stopka, and I. Micek (1999), Experimental verification of the Einstein A-coefficient used for evaluation of $O_2(a^1\Delta_g)$ concentration in the chemical oxygen-iodine laser, *J. Phys. B At. Mol. Opt. Phys.*, *32*, 1885–1892, doi:10.1088/0953-4075/32/8/309.

Stamnes, K., S.-C. Tsay, W. Wiscombe, and K. Jayaweera (1988), Numerically stable algorithm for discrete-ordinate-method radiative transfer in multiple scattering end emitting layered media, *Appl. Opt.*, *27*, 2502–2509, doi:10.1364/AO.27.002502.

Thomas, R. G., and B. A. Thrush (1977), Energy transfer in the quenching of singlet molecular oxygen: I. Kinetics of quenching of singlet oxygen, *Proc. R. Soc. London, Ser. A*, *356*, 287–294, doi:10.1098/rspa.1977.0133.

Titov, D. V., et al. (2006), Venus Express science planning, *Planet. Space Sci.*, *54*, 1279–1297, doi:10.1016/j.pss.2006.04.017.

Tsang, C. C. C., P. G. J. Irwin, F. W. Taylor, and C. F. Wilson (2008), A correlated-k model of radiative transfer in the near-infrared windows of Venus, *J. Quant. Spectrosc. Radiat. Transfer*, *109*, 1118–1135.

Vallance Jones, A., and A. W. Harrison (1958), $^1\Delta_g - X^3\Sigma_g^- O_2$ infrared emission band in the twilight airglow spectrum, *J. Atmos. Terr. Phys.*, *13*, 45–60, doi:10.1016/0021-9169(58)90024-2.

Winick, J. R., R. H. Picard, R. D. Sharma, and R. M. Nadile (1985), Oxygen singlet Delta 1.58-μm (0–1) limb radiance in the upper stratosphere and lower mesosphere, *J. Geophys. Res.*, *90*, 9804–9814, doi:10.1029/JA090iA10p09804.

Zasova, L., et al. (2007), Structure of the Venus atmosphere, *Planet. Space Sci.*, *55*, 1712–1728, doi:10.1016/j.pss.2007.01.011.

A. Cardesin-Moinelo, A. Migliorini, and G. Piccioni, INAF, Istituto di Astrofisica Spaziale e Fisica Cosmica, via del Fosso del Cavaliere 100, I-00133 Rome, Italy. (Giuseppe.piccioni@iasf-roma.inaf.it)

P. Drossart, LESIA, Observatoire de Paris, UPMC, Université Paris-Diderot, CNRS, 5 place Jules Janssen, F-92195 Meudon, France.

F. P. Mills and A. García Muñoz, Research School of Physics and Engineering, Australian National University, Canberra, ACT 0200, Australia.

A. Shakun and L. Zasova, Space Research Institute of Russian Academy of Sciences, Profsojuznaja 84/32, 117997 Moscow, Russia.